Department of Exploration Geophysics

Elastic Wave Attenuation, Dispersion and Anisotropy in Fractured Porous Media

Robert J Galvin

This thesis is presented for the Degree of
Doctor of Philosophy
of
Curtin University of Technology

March 2007

Declaration

To the best of my knowledge and belief this thesis contains no material previously published by any other person except where due acknowledgment has been made.

This thesis contains no material which has been accepted for the award of any other degree or diploma in any university.

Signature: R. Galvin

Date: 4/12/07

Abstract

Development of a hydrocarbon reservoir requires information about the type of fluid that saturates the pore space, and the permeability distribution that determines how the fluid can be extracted. The presence of fractures in a reservoir can be useful for obtaining this information. The main objectives of this thesis are to investigate how fracturing can be detected remotely using exploration seismology. Fracturing will effect seismic data in a number of ways. Firstly, if the fractures are aligned preferentially in some direction, the medium will exhibit long wavelength anisotropy. In turn, if wave propagation is not aligned with one of the symmetry axes of the effective medium then shear wave splitting will depend upon the properties of the fracture filling fluid. Secondly, elastic waves will experience attenuation and dispersion due to scattering and wave-induced fluid flow between the fractures and matrix porosity. This occurs because the fractures are more compliant than the background medium and therefore there will be a pressure gradient formed during passage of the wave, causing fluid to flow between fractures and background.

If the direction of shear-wave propagation is not perpendicular or parallel to the plane of fracturing, the wave polarized in the plane perpendicular to the fractures is a quasi-shear mode, and therefore the shear-wave splitting will be sensitive to the fluid bulk modulus. The magnitude of this sensitivity depends upon the extent to which fluid pressure can equilibrate between pores and fractures during the period of the deformation. In this thesis I use the anisotropic Gassmann equations and existing formulations for the excess compliance due to fracturing to estimate the splitting of vertically propagating shear-waves as a function of the fluid modulus for a porous medium with a single set of dipping fractures and with two conjugate fracture sets dipping with opposite dips to the vertical. This is achieved using two alternative approaches. In the first approach it is assumed that the deformation taking place is quasi-static. That is, the frequency of the elastic disturbance is low enough to allow enough time for fluid to flow between both the fractures and the pore space throughout the medium. In the second approach

I assume that the frequency is low enough to allow fluid flow between a fracture set and the surrounding pore space, but high enough so that there is not enough time during the period of the elastic disturbance for fluid flow between different fracture sets to occur. It is found that the second approach yields a much stronger dependency of shear-wave splitting on the fluid modulus than the first one. This is a consequence of the fact that at higher wave frequencies there is not enough time for fluid pressure to equilibrate and therefore the elastic properties of the fluid have a greater effect on the magnitude of the shear-wave splitting. I conclude that the dependency of the shear-wave splitting on the fluid bulk modulus will be at its minimum for quasi-static deformations, and will increase with increasing wave frequency.

In order to treat the problem of dispersion and attenuation due to wave-induced fluid flow I consider interaction of a normally incident time-harmonic longitudinal plane wave with a circular crack imbedded in a porous medium governed by Biot's equations of dynamic poroelasticity. The problem is formulated in cylindrical coordinates as a system of dual integral equations for the Hankel transform of the wave field, which is then reduced to a single Fredholm integral equation of the second kind. It is found that the scattering that takes place is predominantly due to wave induced fluid flow between the pores and the crack. The scattering magnitude depends on the size of the crack relative to the slow wave wavelength and has it's maximum value when they are of the same order. I conclude that this poroelastic effect should not be neglected, at least at seismic frequencies.

Using the solution of the scattering problem for a single crack and multiple-scattering theory I estimate the attenuation and dispersion of elastic waves taking place in a porous medium containing a sparse distribution of such cracks. I obtain from this analysis an effective velocity which at low frequencies reduces to the known static Gassmann result and a characteristic attenuation peak at the frequency such that the crack size and the slow wave wavelength are of the same order. When comparing with a similar model in which multiple scattering effects are neglected I find that there is agreement

at high frequencies and discrepancies at low frequencies. I conclude that the interaction between cracks should not be neglected at low frequencies, even in the limit of weak crack density. Since the models only agree with each other at high frequencies, when the time available for fluid diffusion is small, I conclude that the interaction between cracks that takes place as a result of fluid diffusion is negligible at high frequencies. I also compare my results with a model for spherical inclusions and find that the attenuation for spherical inclusions has exactly the same dependence upon frequency, but a difference in magnitude that depends upon frequency. Since the attenuation curves are very close at low frequencies I conclude that the effective medium properties are not sensitive to the shape of an inclusion at wavelengths that are large compared to the inclusion size. However at frequencies such that the wavelength is comparable to or smaller than the inclusion size the effective properties are sensitive to the greater compliance of the flat cracks, and more attenuation occurs at a given frequency as a result.

Acknowledgements

I would like to thank my supervisor, Professor Boris Gurevich, for his guidance and for always being available for stimulating discussions. The considerable amount of time he put into assisting me with this work is greatly appreciated. I would like to thank Colin M. Sayers for his input and useful discussions about the research presented in Chapter 3. I also thank Radim Ciz and Julianna Toms for allowing me to use their MATLAB code for the spherical inclusion comparison in Chapter 5. I also thank CSIRO Petroleum for giving me time to complete this thesis.

This research was financially supported by the Minerals and Energy Research Institute of Western Australia, the Australian Petroleum Production and Exploration Association (K. A. Richards Memorial Scholarship), the Australian Research Council, Project DP0342998, the American Association of Petroleum Geologists (Sherman A. Wengerd Memorial Grant), Curtin University's Department of Exploration Geophysics, the Curtin Reservoir Geophysics Consortium and an Australian Postgraduate Award.

Contents

List of Figures

Chapter 1

Introduction

1.1 Motivation

Development of a hydrocarbon reservoir requires information about the type of fluid that saturates the pore space, and the permeability that determines how easily the fluid can be extracted. The presence of fractures in a reservoir can be useful for obtaining this information. If the response of the fractures to elastic deformation is dependent upon the properties of the fluid occupying the fracture porosity we may be able to deduce the nature of this fluid using seismic investigations. Additionally, if the fractures are open their presence can significantly increase the effective permeability of the reservoir as they will provide a pathway for fluid flow between regions that may have been unconnected in the absence of fracturing. Knowledge of the orientation of the fractures can be obtained from seismic data, which will allow the design of a drilling program to penetrate the plane of the fracturing and therefore eliminate the need to drill multiple wells into hydraulically isolated regions of the reservoir.

Fractured reservoirs have been classified according to how the fracturing influences the quality of the reservoir. Relating the porosity and permeability contributions of the matrix and the fractures, Nelson (2001) recognises four types of fractured reservoir. Type I reservoirs have a fracture system that contributes reservoir storage, porosity and

permeability. Type II reservoirs have a matrix that contributes reservoir storage and porosity. The fracture system contributes the required permeability to an otherwise unproductive reservoir. Type III reservoirs have a matrix that contributes reservoir storage, porosity and permeability. The fracture system contributes additional permeability to a productive reservoir. Type IV reservoirs have a fracture system that forms impermeable barriers, inhibits fluid flow and causes reservoir anisotropy. The fractures contribute no additional porosity or permeability. The fractured reservoirs I am interested in are those of Type II, where the fracturing is required to make production economical.

1.2 Aim

The main objectives of this thesis are to investigate how fracturing can be detected remotely using exploration seismology. Fracturing will effect seismic data in a number of ways. Firstly, if the fractures are aligned preferentially in some direction, the medium will exhibit long wavelength anisotropy. In turn, if wave propagation is not aligned with one of the symmetry axes of the effective medium then shear wave splitting will depend upon the properties of the fracture filling fluid. Secondly, elastic waves will experience attenuation and dispersion due to scattering and wave-induced fluid flow between the fractures and matrix porosity. This occurs because the fractures are more compliant than the background medium and therefore there will be a pressure gradient formed during passage of the wave, causing fluid to flow between fractures and background.

1.3 Previous Work

There are two primary methods used to model fracturing of a medium. "Linear slip" theory treats fractures as being planes of weakness across which displacement discontinuities may occur, and gives effective medium properties based on the assumption of a linear relationship between traction and displacement discontinuity (slip) across the fracture.

"Penny-shaped" crack theory simulates fracturing using a distribution of very thin oblate spheroidal inclusions containing a material that is more compliant than the background. Effective medium properties are obtained by considering the scattering from a single crack and using a multiple-scattering theorem to estimate the effect of a distribution of cracks.

1.3.1 Linear slip theory

The general linear-slip model of the elastic medium with parallel fractures has been formulated in terms of the excess compliance that exists due to the presence of weak planar fracturing (Schoenberg & Douma (1988); Schoenberg & Sayers (1995); Sayers & Kachanov (1995)). One of it's advantages is that it requires no assumptions regarding the microscopic details of the fracturing. The excess compliance that defines the fracturing is determined using physically intuitive relationships between stress and displacement discontinuity across the fractures.

Since in the low-frequency limit a linear-slip medium is equivalent to one with transverse isotropy, Gurevich (2003) was able to derive expressions for the low-frequency elastic constants of the fractured porous medium saturated with a given fluid using the anisotropic Gassmann (1951) equations of static poroelasticity. Brajanovski et al. (2005) model a fractured medium as very thin, highly porous layers in a porous background. Their model implies that these fractures are of infinite extent and therefore is valid when fracture spacing is much smaller than fracture length (diameter). This model uses Biot's equations of dynamic poroelasticity, and so frequency effects can be analysed.

1.3.2 Penny-shaped crack theory

The problem of scattering by a crack in an elastic medium has been investigated previously (Robertson (1967); Garbin & Knopoff (1973); Piau (1979)). In particular, Robertson (1967) formulated this problem in cylindrical co-ordinates as a system of dual integral equations in the Hankel transform of the wave field, which was then reduced to a Fred-

holm equation of the second kind. The overall elastic properties of a medium containing a distribution of cracks was treated by Hudson (1980).

In the limit of low frequencies static models can be used to obtain the effective elastic moduli of the fluid-saturated medium in terms of the properties of the dry skeleton and the saturating fluid (Gassmann (1951); Brown & Korringa (1975); Thomsen (1995); Gurevich (2003); Cardona (2002)). For these models to be valid, fluid pressure must have time to fully equilibrate throughout the connected porespace which will only be the case at low frequencies. At higher frequencies pressure equlibration will be incomplete causing frequency dependent attenuation and dispersion. The analysis of these effects require a dynamic model of interaction of an elastic wave with an ensemble of fractures in a porous medium.

A number of schemes tackling this dynamic problem in fractured porous rocks are currently available. The case of finite-size fractures was considered by Hudson et al. (1996), who model fractures as thin penny-shaped voids, and account for fluid flow effects by applying the diffusion equation to a single crack and ignoring interaction between cracks (referred to as the equant porosity model, EPM, later in the thesis). This approximation however leads to some unphysical effects, such as the result that the anisotropy of the fluid-saturated fractured and porous rock in the low frequency limit is the same as for the dry rock (Hudson et al. (2001); Chapman (2003); Brown & Gurevich (2004)).

Maultzsch et al. (2003) analyse frequency-dependent anisotropy caused by the presence of meso-scale fractures in a porous rock, by considering connectivity of individual fractures, pores and microcracks. A more general computational model which can take account of pores and fractures of any size and shape was proposed by Jakobsen et al. (2003) using the T-matrix approximation, commonly used to study effective properties of heterogeneous media. In the T-matrix approximation the effect of voids (pores, fractures) is introduced as a perturbation of the solution for the elastic background medium.

An alternative approach is to model the effect of fractures as a perturbation with respect to an isotropic porous background medium. This approach seems attractive

because it allows us to use all the machinery of the theory of wave propagation in fluid-saturated porous media, known as the theory of poroelasticity ((Biot, 1962)), without specifying individual shapes of grains or pores. It also seems logical to assume that the perturbation of the porous medium caused by the introduction of fractures will be much smaller than the perturbation caused by putting all the pores and fractures into an elastic solid. Recently, similar problems have been investigated in the fields of poroelasticity and the mathematically analogous thermoelasticity. Jin & Zhong (2002) investigated the dynamic stress intensity factor of a circular crack in an infinite poroelastic solid, however they only treated the case of impermeable crack surfaces. Sherief & El-Maghraby (2003) solve a dynamical problem for an infinite thermoelastic solid with an internal circular crack which is subjected to prescribed temperature and stress distributions.

1.4 Thesis Structure

The second chapter of this thesis provides a theoretical background to the techniques employed in later chapters. In Chapter 3 the dependency of shear-wave splitting on the elastic properties of the fracture-filling fluid is investigated. In Chapter 4 I consider interaction of a normally incident time-harmonic longitudinal plane wave with a circular crack imbedded in a porous medium governed by Biot's equations of dynamic poroelasticity. Chapter 5 contains the derivation of the long wavelength effective medium properties that can be obtained using the single scattering solution of Chapter 4 and a multiple-scattering theorem. Conclusions and Recommendations follow in Chapter 6.

Chapter 2

Background Theory

In this Chapter I provide a background to the existing theory that is used in Chapters 3-5.

2.1 Elastic Properties of Fractured Media

The most general way to describe the effect of fractures in an elastic medium is to specify overall weakness or compliance that they give to the host medium. Following the formulation of Sayers & Kachanov (1995), the elastic compliance of a fractured medium may be expressed in the tensor form,

$$S_{ijkl} = S^0_{ijkl} + \Delta S_{ijkl}, \tag{2.1}$$

where S^0_{ijkl} is the elastic compliance tensor of the unfractured background medium, and ΔS_{ijkl} is the excess compliance due to the presence of fractures. When fracture interactions and pressure communication between fractures can be neglected, i.e., for moderate fracture densities, the excess compliance ΔS_{ijkl} may be expressed as

$$\Delta S_{ijkl} = \frac{1}{4}\left(\delta_{ik}\alpha_{jl} + \delta_{il}\alpha_{jk} + \delta_{jk}\alpha_{il} + \delta_{jl}\alpha_{ik}\right) + \beta_{ijkl}. \tag{2.2}$$

Here α_{ij} is a second-rank tensor and β_{ijkl} is a fourth-rank tensor, defined by

$$\alpha_{ij} = \frac{1}{V} \sum_r B_T^{(r)} n_i^{(r)} n_j^{(r)} A^{(r)}, \tag{2.3}$$

$$\beta_{ijkl} = \frac{1}{V} \sum_r \left(B_N^{(r)} - B_T^{(r)} \right) n_i^{(r)} n_j^{(r)} n_k^{(r)} n_l^{(r)} A^{(r)}. \tag{2.4}$$

$B_N^{(r)}$ and $B_T^{(r)}$ are the normal and shear compliances of the rth fracture in volume V, $n_i^{(r)}$ is the ith component of the normal to the fracture, $A^{(r)}$ is the area of the fracture, and δ_{mn} is Kronecker's delta (Sayers & Kachanov, 1995). Without the assumption of no fracture interaction, $B_N^{(r)}$ and $B_T^{(r)}$ would themselves depend upon $n_i^{(r)}$. The tangential compliance is assumed to be independent of the direction of the shear traction that occurs within the plane of the fracture. This implies that each fracture set is, on average, rotationally symmetric. This means that the present theory may not be applicable to large-scale joints (which are bed-limited in height, but may be very long). However, it has been shown (Grechka & Kachanov, 2006) that fractures with random in-plane irregularities are adequately represented by rotationally invariant ones. It is important to note that α_{ij} and β_{ijkl} are symmetric with respect to all rearrangements of the indices. The stiffness tensor for a medium of any desired symmetry can be found by inverting the compliance tensor (2.1).

2.2 Effect of Porosity and Fluid

If the fractures are embedded in a porous, permeable and fluid-saturated background, they can no longer be described by the above formalism, as the effect of fractures will be influenced by the fluid flow between pores and fractures. However the above formalism can still be used to describe the properties of the dry medium. The stiffness matrix of the dry medium is here defined as c_{ij}^{dry} using the conventional two-subscript 6×6 matrix notation (Nye, 1985). For low frequencies the stiffness matrix c_{ij}^{sat} of the fluid-

saturated medium can be related to the bulk modulus of the solid grain material K_g, fluid bulk modulus K_f, and porosity ϕ of the isotropic background medium using the anisotropic version of the Gassmann equations (Gassmann (1951); Brown & Korringa (1975); Gurevich (2003)),

$$c_{ij}^{sat} = c_{ij}^{dry} + \frac{\alpha}{D^*} b_i b_j, \qquad i,j = 1,2,...,6 \tag{2.5}$$

where

$$b_i = \varepsilon_i - \frac{c_{1i}^{dry} + c_{2i}^{dry} + c_{3i}^{dry}}{3K_g}, \qquad i = 1,2,...,6, \tag{2.6}$$

$$D^* = 1 + \frac{\alpha}{3K_g}\left(b_1 + b_2 + b_3\right), \tag{2.7}$$

$$\frac{1}{\alpha} = \phi\left(\frac{1}{K_f} - \frac{1}{K_g}\right), \tag{2.8}$$

and

$$\begin{aligned} \epsilon_1 = \epsilon_2 = \epsilon_3 = 1 \\ \epsilon_4 = \epsilon_5 = \epsilon_6 = 0. \end{aligned} \tag{2.9}$$

2.3 Effect of Frequency

The description of the effects of fractures given above is applicable in the low-frequency limit, that is, when both the wavelength and the fluid diffusion length are much larger than the size of the pores and fractures. When we look at higher frequencies, we must take into account the actual finite geometry of the fractures in order to obtain effective medium properties. The simplest geometry that can be used to represent fracturing is the flat, circular (or "penny-shaped") crack. This crack geometry is effectively an oblate spheroid. The ingredient required to obtain effective medium properties for a distribution of such cracks is the solution for scattering from a single crack. The classical problem of scattering from a single crack embedded in an elastic medium was solved by Robertson (1967).

He considered an incident plane normal compressional wave propagating in an elastic medium along the z-axis of a cylindrical co-ordinate system with the axial displacement $u_z^{in} = u_0 e^{ik_1 z}$, where k_1 is the wavenumber (time dependency $e^{-i\omega t}$ is assumed). He obtained the secondary (scattered) field $\mathbf{u}(\mathbf{r})$ resulting from interaction of the incident wave with the crack occupying the circle $r \leq a$ in the plane $z = 0$. The total field is therefore $\mathbf{u}^T(\mathbf{r}) = u_z^{in}\mathbf{e}_z + \mathbf{u}(\mathbf{r})$, where $\mathbf{e}_z$ is a unit vector in the z-direction. Both the scattered and total fields must each satisfy the following equation of elasticity in the semi-infinite elastic medium $z \geq 0$:

$$(\lambda + 2\mu)\nabla\nabla \cdot \mathbf{u} - \mu\nabla \times \nabla \times \mathbf{u} + \boldsymbol{\rho\omega}^2\mathbf{u} = \mathbf{0}, \tag{2.10}$$

where λ and μ are the elastic constants, ω is the angular frequency and ρ is the density.

The distribution of displacements and stresses, σ_{ij}, in the neighborhood of the crack is the same as that produced in a semi-infinite elastic medium $z \geq 0$ when its free surface is subject to the following boundary conditions:

$$\sigma_{rz} = 0 \qquad 0 \leq r < \infty, \tag{2.11}$$

$$\sigma_{zz} = p_0 \qquad 0 \leq r < a, \tag{2.12}$$

$$u_z = 0 \qquad r > a, \tag{2.13}$$

where p_0 is the incident pressure. The general solution of the equation of motion in cylindrical coordinates can be obtained by representing the two axial and radial components u_z and u_r of the displacements in the form of an inverse Hankel transform with respect to the radial coordinate r, e.g.

$$u_i(z, r) = \int_0^\infty \widetilde{u}_i(z, y) y J_0(yr) dy \qquad i = z, r. \tag{2.14}$$

Substitution of these representations into the equation of motion (2.10) yields a system

of ordinary second-order differential equations with constant coefficients for the functions $u_i(z,r)$, in the independent variable z with radial wave number y as a parameter. These equations can be readily integrated, giving general solutions of the form

$$\widetilde{u}_i(z,y) = A_{i1}(y)e^{-q_i z} + A_{i2}(y)e^{-q_2 z}, \tag{2.15}$$

where q_1 and q_2 are vertical wavenumbers of the compressional and shear waves respectively. Then boundary conditions (2.11)-(2.13) yield a system of integral equations for the unknown wave amplitudes $A_{ij}(y)$. The condition (2.11) can be used to eliminate the shear wave amplitude, resulting in the following system of dual integral equations for the normal compressional wave amplitude $B(y) = 2\mu(1-g)k_s^2 y(2y^2 - k_s^2)^{-1}A_{z1}(y)$:

$$\int_0^\infty y\,[1+T(y)]\,B(y)J_0\,(yr)\,dy = -p_0 \qquad 0 \le r \le a, \tag{2.16}$$

$$\int_0^\infty B(y)J_0\,(yr)\,dy = 0 \qquad a < r < \infty, \tag{2.17}$$

where $T(y)$ is a known transfer function between stress and displacement arising from the mixed nature of the boundary conditions, J_0 is the zero order Bessel function of the first kind, k_s is the shearwave wavenumber and $g = \mu/(\lambda + 2\mu)$.

As shown by Noble (1963), if $T(y)$ tends to zero as y tends to infinity then

$$B(y) = \frac{2}{\pi}\int_0^a \theta(\xi)\sin(\xi y)d\xi, \tag{2.18}$$

where $\theta(\xi)$ satisifes the Fredholm equation of the second kind

$$\theta(z) + \frac{1}{\pi}\int_0^a M(z,\xi)\theta(\xi)d\xi = -p_0 z, \tag{2.19}$$

and

$$M(z,\xi) = \pi(z\xi)^{\frac{1}{2}}\int_0^\infty yT(y)J_{\frac{1}{2}}(zy)J_{\frac{1}{2}}(\xi y)dy. \tag{2.20}$$

2.4 Multiple Scattering

Using the solution of the problem of scattering of an elastic wave by a single crack, I can obtain the approximate properties of a medium containing a system of randomly placed but perfectly aligned cracks. When one has a distribution of cracks, to obtain effective medium properties one must take into account the multiple events of scattering that will take place. The multiple scattering theorem of Waterman & Truell (1961) provides the method to compute attenuation and dispersion of elastic waves propagating in a medium with randomly distributed inhomogeneities. According to Waterman & Truell (1961), effective wave number may be calculated from the amplitudes of the scattered field as

$$\left(\frac{k^*}{k_1}\right)^2 = \left[1 + \frac{2\pi n_0 f(0)}{k_1^2}\right]^2 - \left[\frac{2\pi n_0 f(\pi)}{k_1^2}\right]^2, \tag{2.21}$$

where k_1 is the real wave number of the fast compressional wave, n_0 is the density or number of scatterers per unit volume and $f(0)$, $f(\pi)$ are amplitudes of the wave scattered in the forward and backward direction (with respect to the incident wave) by a single inclusion. For a sufficiently small concentration of inclusions the quadratic terms in (2.21) can be neglected, which yields

$$k^* = k_1 \left[1 + \frac{4\pi n_0 f(0)}{k_1^2}\right]^{1/2} \approx k_1 \left[1 + \frac{2\pi n_0 f(0)}{k_1^2}\right]. \tag{2.22}$$

The real part of (2.22) gives the effective velocity v^* in media with a low concentration of scatterers

$$\frac{1}{v^*} = \frac{1}{v_1}\left[1 + \frac{2\pi n_0}{k_1^2}\,\mathrm{Re}\left\{f(0)\right\}\right]. \tag{2.23}$$

The imaginary part of (2.22) gives the dimensionless attenuation (inverse quality factor)

$$Q^{-1} = \frac{4\pi n_0}{k_1^2}\,\mathrm{Im}\left\{f(0)\right\}. \tag{2.24}$$

2.5 Biot's Equations of Dynamic Poroelasticity

When we wish to allow for the effect of background porosity and fluid at higher frequencies, we can no longer use the static formulation of Gassmann (1951). At sufficiently high frequencies fluid pressure does not have time to fully equilibrate throughout the connected porespace and there will be dispersion and attenuation taking place due to wave-induced fluid flow. To model these effects we must use a dynamic model of mechanical behaviour in an isotropic fluid-saturated porous medium. The governing equations I use to model wave propagation in fluid-saturated porous media are those of Biot (1962):

$$\nabla \cdot \boldsymbol{\sigma} = -\omega^2 \left(\rho \mathbf{u} + \rho_f \mathbf{w}\right), \tag{2.25}$$

$$\nabla p = \omega^2 \left(\rho_f \mathbf{u} + q\mathbf{w}\right), \tag{2.26}$$

where $\mathbf{w} = \phi\left(\mathbf{U} - \mathbf{u}\right)$ is the relative fluid displacement, ϕ is the medium porosity, $\mathbf{U}$ is the average absolute fluid displacement, ω is the angular wave frequency, ρ_f and ρ are the densities of the fluid and of the overall medium (Biot, 1962). At low frequencies $q\left(\omega\right) \approx i\eta/\kappa\omega$ (Biot, 1956) is a frequency-dependent coefficient responsible for viscous and inertial coupling between the solid and fluid displacements where η is the fluid viscosity and κ is the intrinsic permeability of the medium. $\boldsymbol{\sigma}$ and p are the total stress tensor and fluid pressure, which are related to the displacement vectors via the constitutive relations

$$\boldsymbol{\sigma} = \left[\left(H - 2\mu\right)\nabla \cdot \mathbf{u} + \alpha M \nabla \cdot \mathbf{w}\right]\mathbf{I} + \mu\left[\nabla\mathbf{u} + \left(\nabla\mathbf{u}\right)^T\right], \tag{2.27}$$

$$p = -\alpha M \nabla \cdot \mathbf{u} - M \nabla \cdot \mathbf{w}. \tag{2.28}$$

In equations (2.27) and (2.28) μ is the shear modulus of the solid frame, $\alpha = 1 - K/K_g$ is the Biot-Willis coefficient (Biot & Willis, 1957),

$$M = \left[\frac{(\alpha - \phi)}{K_g} + \frac{\phi}{K_f} \right]^{-1} \tag{2.29}$$

is the so-called pore space modulus,

$$H = K_{sat} + \frac{4}{3}\mu \tag{2.30}$$

is the P-wave modulus of the saturated poroelastic medium and K_{sat} is the bulk modulus of the saturated medium which is related to the bulk moduli of the fluid K_f, solid K_g, and dry skeleton K by the Gassmann (1951) equation

$$K_{sat} = K + \alpha^2 M. \tag{2.31}$$

In the next chapter I will analyse the dependency of shear-wave splitting on the fluid filling the fractures that give rise to effective anisotropy.

Chapter 3

Fluid-dependent Shear-wave Splitting in a Fractured Poroelastic Medium

3.1 Introduction

Naturally fractured reservoirs are becoming increasingly important for oil and gas exploration in many areas of the World. The presence of aligned fractures in a reservoir can be a main cause of azimuthal anisotropy of its elastic properties. There is, therefore, considerable interest in the use of measurements of seismic anisotropy to estimate the orientation and density of fracture networks. One of the methods used to estimate seismic anisotropy relies on measuring the magnitude of shear-wave splitting, that is, the time delay between two shear-waves propagating in the same direction with different polarizations (e.g. Crampin (1985)). According to commonly used fracture models (Hudson (1980); Schoenberg (1980)), in a medium permeated by fractures that are aligned parallel to a single vertical plane, vertical shear-wave splitting is independent of the fluid fill and can be used as a direct indicator of fracture density. However, recently, for a relatively thick fractured carbonate, a higher shear-wave splitting and a lower shear-wave velocity

were observed in the gas-saturated region of the reservoir than the oil-saturated region (Guest et al. (1998); van der Kolk et al. (2001)). These results suggest the sensitivity of shear-wave splitting to the fluid type in fractured media.

A number of possible explanations of this phenomenon have been proposed. In particular, Guest et al. (1998) and van der Kolk et al. (2001) suggested that the effect of fluid on shear-wave splitting is caused by the frequency dependence of seismic velocities in a medium with large fracture density (this explanation is challenged by Hudson & Crampin (2003).) Bakulin et al. (2000b) and Cardona et al. (2001) showed that vertical shear-wave splitting in a medium permeated by vertical fractures will not be influenced by the saturating fluid if the fractures are rotationally symmetric. This is understandable, as in this case both shear-waves are pure modes with velocities dependent only on the tangential fracture compliance B_T, which is independent of the fluid fill (Schoenberg & Douma, 1988). Bakulin et al. (2000b) also showed that even vertical fracturing may lead to fluid-dependent shear-wave splitting if for some reason the fractures are not rotationally invariant. For example, fractures may not be rotationally invariant if a non-hydrostatic stress field acts at an angle to the fracture system (Nakagawa et al., 2000). If, however, the direction of wave propagation is not parallel or perpendicular to the fracturing, the wave polarized in the plane perpendicular to the fractures is a quasi-shear mode, and therefore is also affected by the normal fracture compliance B_N. Consequently, the shear-wave splitting depends on both B_N and B_T. This effect was analysed by Sayers (2002) who showed that shear-wave splitting decreases with decreasing B_N/B_T and this decrease is approximately proportional to the fracture dip. Additionally unlike B_T, normal fracture compliance B_N decreases with increasing fluid bulk modulus in a way that depends on the permeability of the background medium (Hudson (1981); Schoenberg & Douma (1988); Hudson et al. (1996); Pointer et al. (2000); Hudson et al. (2001)). Based on this, Sayers (2002) concluded that fractures filled with higher bulk modulus fluids results in smaller shear-wave splitting.

The results of Sayers (2002) show the trend of shear-wave splitting versus fluid bulk

modulus, but do not give a magnitude or shape of this dependency. Quantitative analysis of this dependency requires an explicit relationship between normal fracture compliance B_N and the bulk modulus of the fluid. For isolated penny-shaped fractures in an elastic medium, these relationships are straightforward: if isolated aligned fractures contain gas, then B_N is expected to be of the same order of magnitude as B_T. If the fluid is liquid (brine, oil), then B_N is expected to be much smaller than B_T (Hudson (1981); Sayers & Kachanov (1995); Schoenberg & Douma (1988)).

More relevant to the petroleum industry are reservoirs containing fractures that are embedded in an already porous background, with pores providing most of the storage and fractures acting as permeability conduits (Hudson, 1981). If the system of pores and fractures in a fluid-saturated rock is interconnected, forming a so-called double-porosity medium, then fluid flow between pores and fractures will affect the overall elastic properties and must be taken into account (O'Connell & Budiansky (1974); Auriault & Boutin (1994); Pride & Berryman (2003)). The effect of such wave-induced fluid flow on elastic properties is frequency dependent. If the wave frequency is sufficiently high, then fluid does not have time to flow between fractures and pores as the wave passes, and the effective medium representation using isolated fractures applies. Conversely, at lower frequencies the fluid pressure has time to partially or fully equilibrate between pores and fractures and theoretical models for fractures in non-porous elastic media do not apply (Thomsen (1995); Hudson et al. (2001)). Therefore, quantitative analysis of the effect of fluid on shear-wave splitting at low (e.g. seismic) frequencies requires an understanding of how the modified elastic properties due to the presence of fractures depend on the background porosity.

It has been understood for some time (Schoenberg & Douma, 1988) that fluid communication between fractures and background porosity results in an increase of the normal excess fracture compliance, B_N. The first quantitative analysis of this effect was performed by Thomsen (1995) who obtained approximate closed-form expressions of fracture-induced anisotropy parameters (related to B_N) as functions of fracture den-

sity, fluid compressibility and background porosity. The results of Thomsen (1995) were derived using a version of self-consistent effective medium theory (Hoenig, 1979) and are limited to small fracture densities. Recently, Gurevich (2003) and Cardona (2002) showed that fracture-induced compliance of fluid-saturated porous media with aligned fractures can be obtained using the anisotropic variant of the Gassmann equations (Gassmann (1951); Brown & Korringa (1975)). An essential feature of this approach is that it gives an exact expression (not limited to small fracture density) for the stiffness tensor as a function of fluid compressibility and porosity, provided the fracture compliances for dry fractured rock are known.

In this chapter I use the anisotropic Gassmann theory described above to quantify the effect of hydraulic interaction on shear-wave splitting. Specifically, I consider the splitting of vertically propagating shear-waves (1) in a porous medium with a single set of dipping fractures and (2) with two oppositely dipping conjugate fracture sets. First, I consider a dry porous medium with a single set of parallel fractures, Figure 3-1, and define its normal and tangential excess fracture compliances B_N and B_T. Using explicit fluid substitution expressions given by Gurevich (2003) I then obtain the stiffness tensor of the same fractured, porous medium but saturated with a fluid. If expressed in the coordinate system associated with the fracture plane, this tensor is transversely isotropic and two shear-wave velocities can be computed as a function of angle between the propagation direction and the normal to the fracture plane. For vertically propagating waves this angle corresponds to the fracture dip. Thus, by calculating the relative difference between orthogonally polarized shear-wave velocities one should be able to obtain the dependence of shear-wave splitting on the fracture dip and fluid bulk modulus.

For a system of two conjugate fracture sets (that is, two oppositely dipping fracture sets, Figures 3-2 and 3-3), I start by defining dry normal and tangential excess fracture compliances B_N and B_T for each of the fracture sets. I explore two alternative workflows. In the first approach, I construct the compliance tensor for the dry medium with two fracture sets. Following Sayers (2002), this is done using the tensor form of the elastic

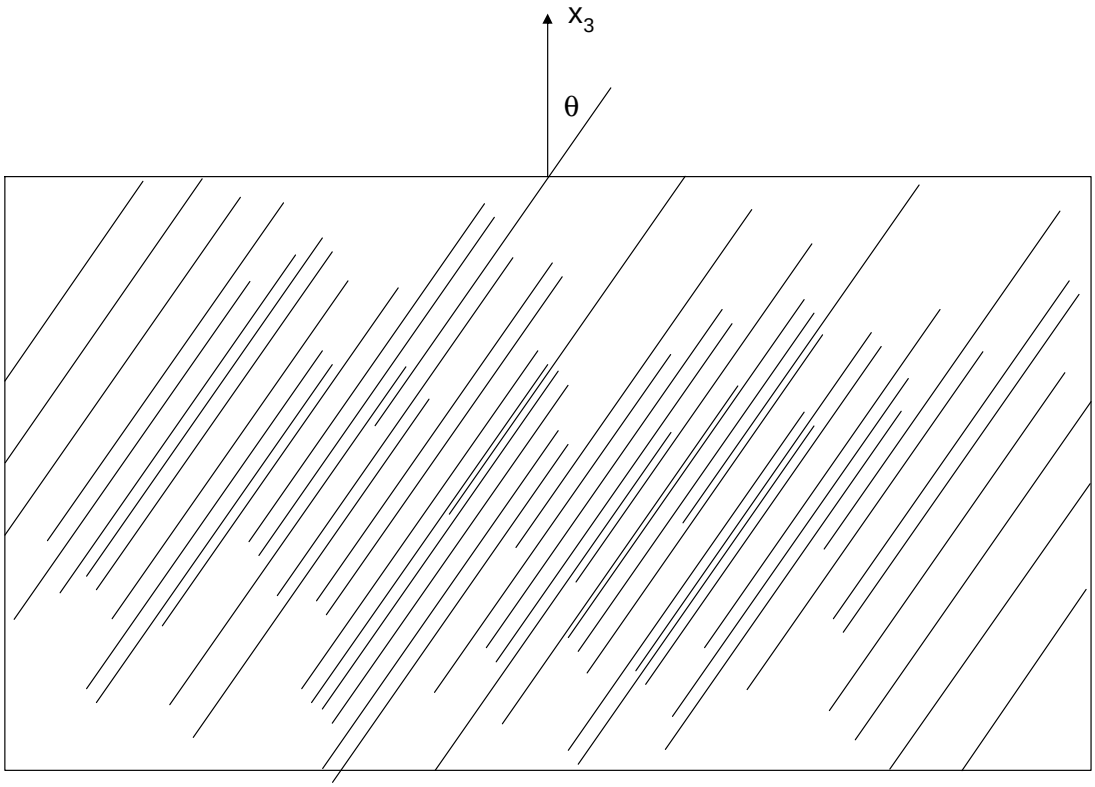

Figure 3-1: A single set of aligned fractures which dip at angle θ with respect to the vertical.

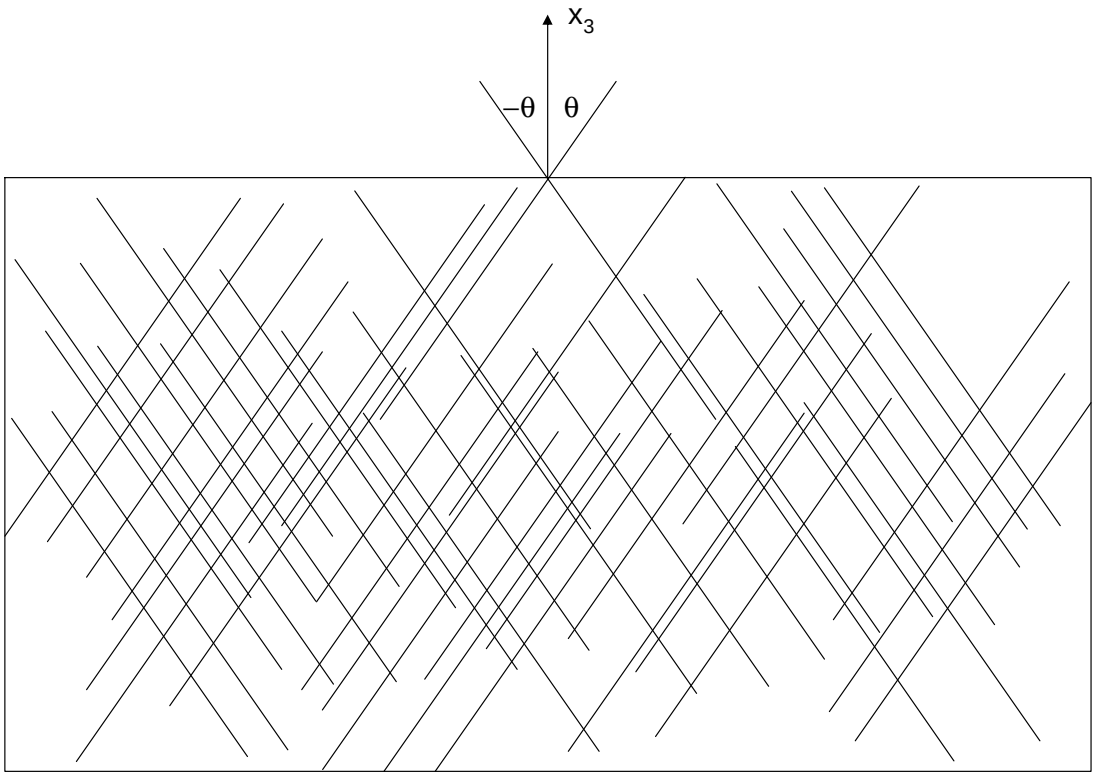

Figure 3-2: Two conjugate sets of aligned fractures which dip at angle θ with respect to the vertical.

linear-slip theory (Sayers & Kachanov, 1995), which is applicable in this case as the medium is dry and therefore elastic. Once the dry stiffness tensor is known, the stiffness of the saturated material is computed using anisotropic versions of the Gassmann (1951) equations. The second alternative is to construct compliance tensors for each fracture set, apply anisotropic Gassmann equations to them separately and only then compute the saturated compliance tensor using the Sayers & Kachanov (1995) formalism. The applicability of each of these two approaches depends on whether or not fluid pressure is equilibrated between the two fracture sets, and hence on the frequency of the elastic disturbance. This is further analysed in the Discussion section.

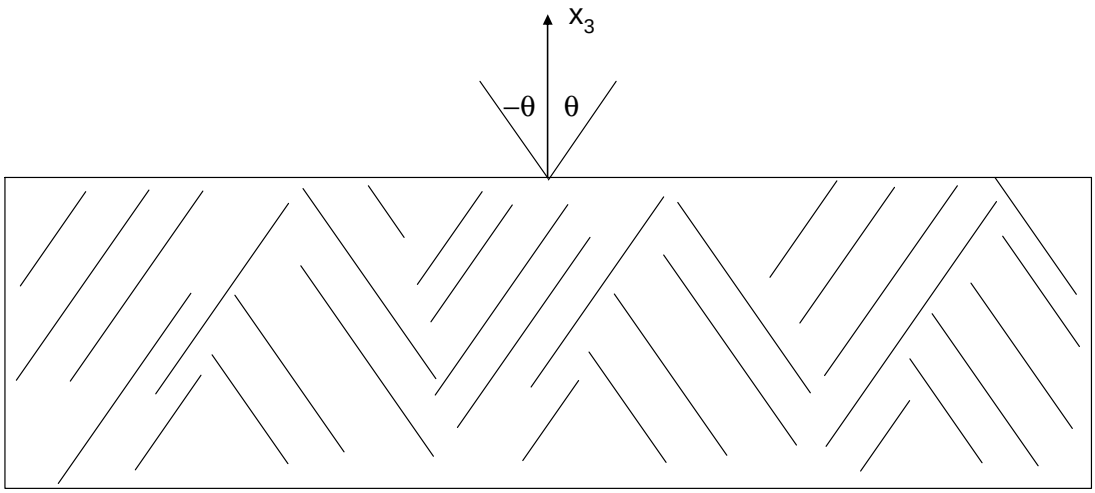

Figure 3-3: Two sets of fractures in which the orientation of neighboring fractures are correlated such that the fracture system can be considered as consisting of domains of aligned fractures.

In the following I use equations (2.1)-(2.4) from Chapter 2 to compute the shear-wave splitting in porous media first with a single fracture set and subsequently with two conjugate fracture sets.

3.2 Shear-wave Splitting in Porous Media with a Single Set of Aligned Fractures

The simplest example of a fractured medium in which splitting of vertically propagating shear-waves is a function of the normal fracture compliance is an isotropic porous background permeated by a set of aligned fractures which dip with respect to the vertical (Figure 3-1). The symmetry of this medium is transverse isotropy with a symmetry plane perpendicular to the fracture set present. In this case, the theory of Sayers & Kachanov (1995) yields explicit expressions for the elastic stiffness tensor of the dry medium derived earlier by Schoenberg & Douma (1988). The elastic stiffness tensor of the dry medium

is given by (Schoenberg & Douma (1988))

$$c_{ij}^{dry} = \begin{bmatrix} L(1-\Delta_N) & \lambda(1-\Delta_N) & \lambda(1-\Delta_N) & 0 & 0 & 0 \\ \lambda(1-\Delta_N) & L\left(1-\left(\frac{\lambda}{L}\right)^2\Delta_N\right) & \lambda\left(1-\frac{\lambda}{L}\Delta_N\right) & 0 & 0 & 0 \\ \lambda(1-\Delta_N) & \lambda\left(1-\frac{\lambda}{L}\Delta_N\right) & L\left(1-\left(\frac{\lambda}{L}\right)^2\Delta_N\right) & 0 & 0 & 0 \\ 0 & 0 & 0 & \mu & 0 & 0 \\ 0 & 0 & 0 & 0 & \mu(1-\Delta_T) & 0 \\ 0 & 0 & 0 & 0 & 0 & \mu(1-\Delta_T) \end{bmatrix} \tag{3.1}$$

in the 6×6 matrix notation where $L=\lambda+2\mu$ is the compressional wave modulus, K and μ are the dry bulk and shear moduli of the background porous rock, and $\lambda = K-\frac{2}{3}\mu$. The effect of the fractures is described in (3.1) through the dimensionless fracture weaknesses Δ_N and Δ_T (Hsu & Schoenberg (1993); Bakulin et al. (2000a)),

$$\Delta_N = \frac{(\lambda+2\mu)B_N}{1+(\lambda+2\mu)B_N}, \tag{3.2}$$

and

$$\Delta_T = \frac{\mu B_T}{1+\mu B_T}, \tag{3.3}$$

where B_N and B_T are normal and tangential fracture compliances in the dry rock, averaged over all sizes and shapes. Equation (3.1) assumes that the fractures are rotationally symmetric, lie in the vertical plane and are perpendicular to the x_1 direction.

To compute the elastic properties of the fluid-saturated medium, the dry stiffness tensor given by equation (3.1) needs to be substituted into the anisotropic Gassmann equations (2.5)-(2.9). This has been done by Gurevich (2003) who derived explicit analytical expressions for the low-frequency elastic stiffness tensor of a saturated porous TI medium as a function of the background porous matrix, the normal and shear fracture excess compliances and the fluid bulk modulus. The five independent components of this

tensor are:

$$c_{11}^{sat} = \frac{L}{D}\left\{d_1\theta + \frac{K_f}{\phi K_g L}\left[L_1\alpha' - \frac{16}{9}\frac{\mu^2\alpha_0}{L}\Delta_N\right]\right\}, \tag{3.4}$$

$$c_{33}^{sat} = \frac{L}{D}\left\{d_2\theta + \frac{K_f}{\phi K_g L}\left[L_1\alpha' - \frac{4}{9}\frac{\mu^2\alpha_0}{L}\Delta_N\right]\right\}, \tag{3.5}$$

$$c_{13}^{sat} = \frac{\lambda}{D}\left\{d_1\theta + \frac{K_f}{\phi K_g \lambda}\left[\lambda_1\alpha' + \frac{8}{9}\frac{\mu^2\alpha_0}{L}\Delta_N\right]\right\}, \tag{3.6}$$

$$c_{44}^{sat} = \mu, \tag{3.7}$$

$$c_{55}^{sat} = \mu\left(1 - \Delta_T\right), \tag{3.8}$$

where

$$D = 1 + \frac{K_f}{K_g\phi}\left(\alpha_0 - \phi + \frac{K^2\Delta_N}{K_g L}\right), \tag{3.9}$$

$$\theta = 1 - \frac{K_f}{K_g}, \tag{3.10}$$

$$\alpha' = \alpha_0 + \frac{K^2}{K_g L}\Delta_N, \tag{3.11}$$

$$L_1 = K_g + \frac{4}{3}\mu, \tag{3.12}$$

$$\lambda_1 = K_g - \frac{2}{3}\mu, \tag{3.13}$$

$$d_1 = 1 - \Delta_N, \tag{3.14}$$

$$d_2 = 1 - \frac{\lambda^2}{L^2}\Delta_N, \tag{3.15}$$

and

$$\alpha_0 = 1 - \frac{K}{K_g}. \tag{3.16}$$

Note that due to the simple TI symmetry of the medium with a single set of fractures, c_{44}^{sat} and c_{55}^{sat} are not affected by the fluid.

Having obtained the stiffness tensor for a fluid-saturated porous TI medium, one can calculate the phase velocity of vertically propagating shear-waves using the equations

(Mavko et al. (1998), adjusted for the different coordinate system used here),

$$V_{S1} = \sqrt{\frac{c_{44}^{sat}\sin^2\theta + c_{55}^{sat}\cos^2\theta}{\rho}}, \tag{3.17}$$

$$V_{S2} = \sqrt{\frac{c_{33}^{sat}\sin^2\theta + c_{11}^{sat}\cos^2\theta + c_{55}^{sat} - \sqrt{M}}{2\rho}}, \tag{3.18}$$

where

$$M = \left[\left(c_{33}^{sat} - c_{55}^{sat}\right)\sin^2\theta - \left(c_{11}^{sat} - c_{55}^{sat}\right)\cos^2\theta\right]^2 + \left(c_{13}^{sat} + c_{55}^{sat}\right)^2\sin^2 2\theta, \tag{3.19}$$

θ is the angle between the wave vector and the axis of symmetry, and ρ is the density of the fluid-saturated medium. Here V_{S1} is the phase velocity of the shear-wave with particle motion parallel to the fracture plane and V_{S2} is the phase velocity of the shear-wave with particle motion having a component perpendicular to the fracture plane. For vertical fractures and vertical propagation, V_{S1}>V_{S2}, although this is not necessarily true at large angles. For an axis of symmetry that is perpendicular to the fracture set, the angle between the fracture set and the vertical is, therefore, $\frac{\pi}{2} - \theta$.

I now illustrate the behavior of the two shear-wave velocities for a medium described by the following properties: $K_g = 70GPa$ (calcite), $\rho_g = 2870kgm^{-3}$, $\phi = 10\%$, $\rho_f = 1kgm^{-3}$, $K_f = 2.25GPa$, $V_P^{dry} = 4000ms^{-1}$, $V_{S1}^{dry} = 1700ms^{-1}$ and $V_{S2}^{dry} = 1445ms^{-1}$. Following Schoenberg & Sayers (1995), I assume as a rough approximation that in the dry rock the normal, B_N, and tangential, B_T, fracture compliances are equal so that β_{ijkl} (2.4) is also zero, simplifying the result. Figure 3-4 shows V_{S1} and V_{S2} versus K_f for vertical propagation and fracture dips ranging from 0° to 90°. Because the particle motion that takes place during the passage of the S_1 wave is parallel to the fracture plane, it is not affected by the presence of fracturing. Particle motion for the S_2 wave is perpendicular to the fracture planes, and therefore V_{S2} is affected by the fracturing. It is apparent from Figure 3-4 that V_{S2} varies with K_f, except for the vertical fracture case.

Figure 3-5 shows the shear-wave splitting parameter, defined as

$$s = \frac{V_{S1}^2 - V_{S2}^2}{V_{S1}^2 + V_{S2}^2}, \tag{3.20}$$

as a function of fluid modulus K_f for the same range of dips as used in Figure 3-4. For vertical fracturing, shear-wave splitting is independent of the fluid bulk modulus, whereas for horizontal fracturing the splitting vanishes because both shear-waves are associated with particle motion in the plane of fracturing. An interesting feature that can be seen in Figure 3-5 for the near-horizontal fracture cases is that the splitting experiences a sign reversal, with the S_2 polarisation achieving a greater phase velocity than the S_1 polarisation. This is, in fact, a common feature of transverse isotropy (Thomsen (1986), Thomsen (1995)).

3.3 Two Conjugate Sets of Fractures

In nature, fractures often occur in two conjugate sets dipping with opposite dips of $\pm\theta$ as shown in Figure 3-2 (Reiss (1980); Nelson (2001)). Such fractures may form due to shear displacement along the fractures, contrasted with extensile displacement of vertical joints. The aim of this section is to analyze the dependency of shear-wave splitting on the fluid bulk modulus for such a system of conjugate fracture sets embedded in a porous and permeable isotropic background rock. This can be done by applying a combination of the Sayers & Kachanov (1995) approach and anisotropic Gassmann equations. I investigate this phenomenon using two alternative approaches.

In the first approach I assume that the deformation is quasi-static, so that at any time the fluid pressure is equilibrated between the two fracture sets and the pores. Thus the elastic properties can be obtained by first computing the stiffness matrix of the dry rock using the Sayers-Kachanov formalism, and then applying anisotropic Gassmann equations to obtain the elastic properties of the fluid saturated rock. This would apply when the two sets of fractures are in full pressure communication, as illustrated in Figure

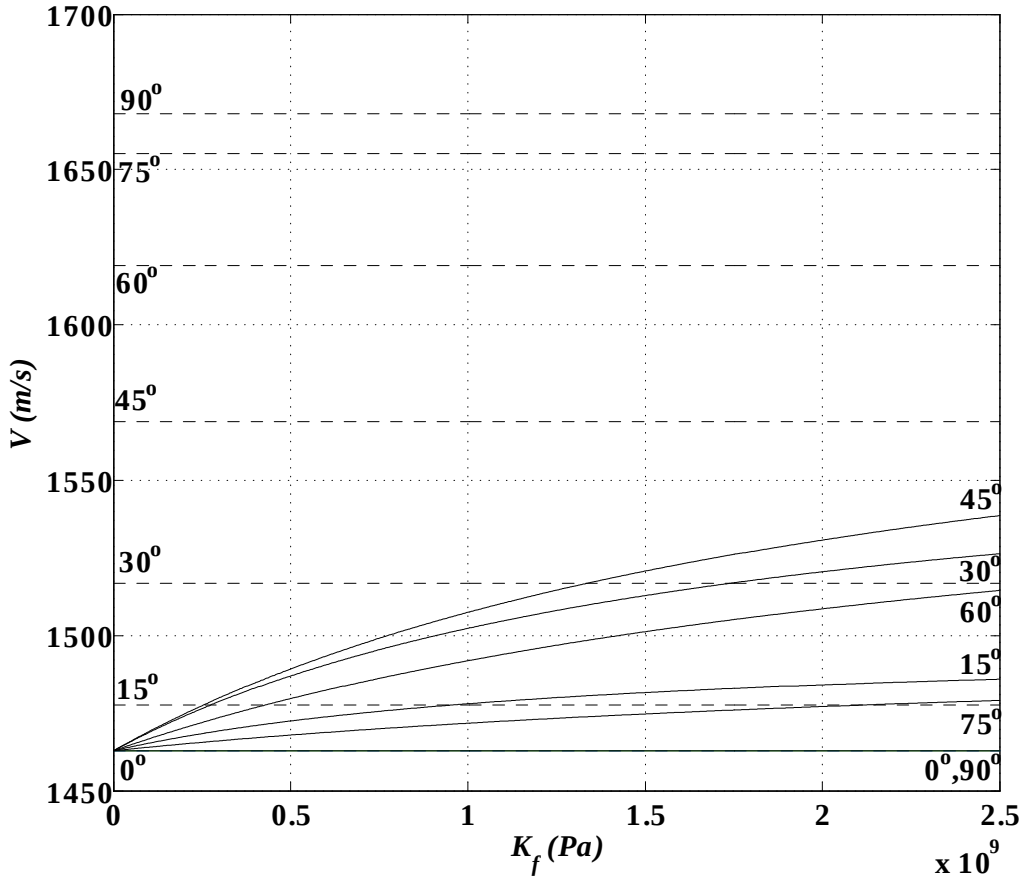

Figure 3-4: V_{S1} (dashed line) and V_{S2} (solid line) vs K_f for the case of a single fracture set and $\theta = 0°, 15°, 30°, 45°, 60°, 75°$ and $90°$. V_{S1} is independent of K_f.

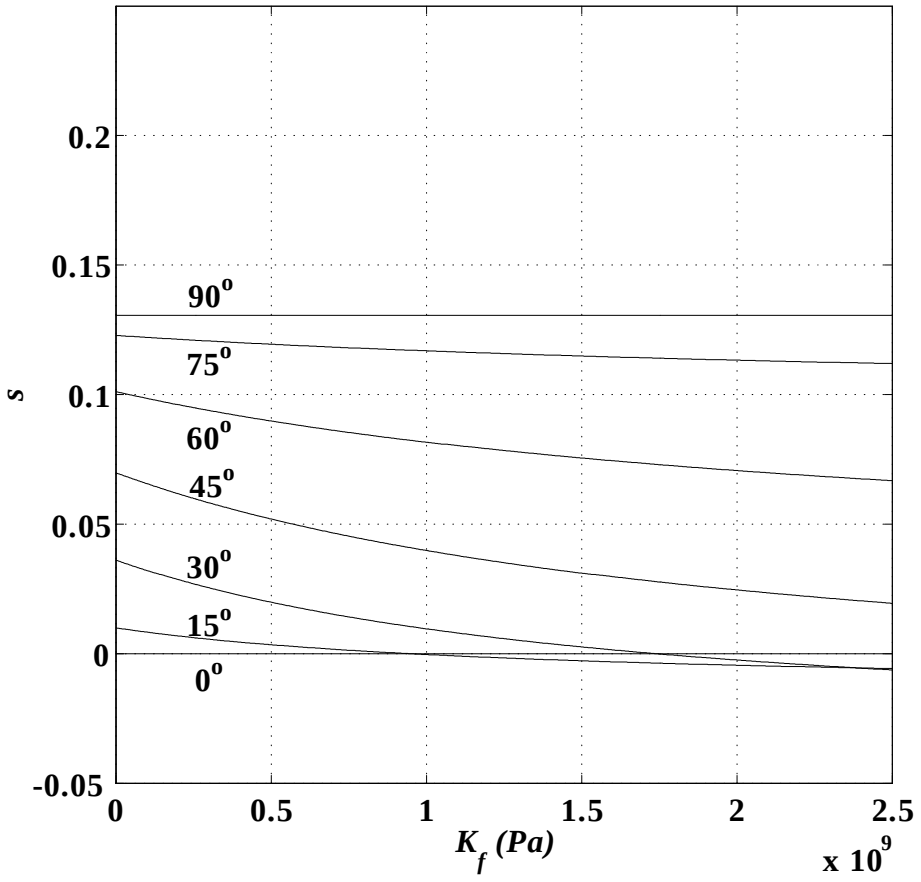

Figure 3-5: s vs K_f for the case of a single fracture set and $\theta = 0°$, 15°, 30°, 45°, 60°, 75° and 90°. For $\theta = 0°$ (horizontal fractures), $s = 0$ whereas for $\theta = 90°$ (vertical fractures), s is not sensitive to K_f. For all other values of θ, s is sensitive to K_f.

3-2. A similar approach for a single set of aligned fractures was suggested by Thomsen (1995). In the second approach I assume that the wave frequency is low enough so that the two fracture sets are in hydraulic equilibrium with the surrounding pore space, but not with each other. I consider the physical meaning of this approach in the Discussion. Thus the saturated fracture compliances may be calculated for each of the two fracture sets individually, and can then be substituted into the Sayers-Kachanov equations (2.1)-(2.4) to compute the overall properties of the saturated fractured system. This approach would apply when the fracture system can be considered as consisting of domains of aligned fractures as illustrated in Figure 3-3. Below I consider these two approaches in greater detail.

3.3.1 Fractures in full pressure equilibrium

A dry rock with two conjugate fracture sets with opposite dips but the same strike can exhibit monoclinic symmetry whereby its elastic tensor takes the form

$$c_{ij} = \begin{bmatrix} c_{11} & c_{12} & c_{13} & 0 & c_{15} & 0 \\ c_{12} & c_{22} & c_{23} & 0 & c_{25} & 0 \\ c_{13} & c_{23} & c_{33} & 0 & c_{35} & 0 \\ 0 & 0 & 0 & c_{44} & 0 & c_{46} \\ c_{15} & c_{25} & c_{35} & 0 & c_{55} & 0 \\ 0 & 0 & 0 & c_{46} & 0 & c_{66} \end{bmatrix}, \tag{3.21}$$

in the 6×6 matrix notation. Note that the coordinate system here is the same as on Figure 3-3. The elements of this matrix can be defined by inverting the compliance matrix obtained using equations (2.1)-(2.4). For two conjugate fracture sets (each rotationally symmetric) the tensors α_{ij} and β_{ijkl} reduce to the form (Sayers, 2002),

$$\alpha_{ij} = A_1 n_i^{(1)} n_j^{(1)} + A_2 n_i^{(2)} n_j^{(2)} \tag{3.22}$$

and

$$\beta_{ijkl} = B_1 n_i^{(1)} n_j^{(1)} n_k^{(1)} n_l^{(1)} + B_2 n_i^{(2)} n_j^{(2)} n_k^{(2)} n_l^{(2)}. \tag{3.23}$$

Here,

$$A_\gamma = \frac{1}{V} \sum_r B_T^{(r)} A^{(r)}, \tag{3.24}$$

and

$$B_\gamma = \frac{1}{V} \sum_r \left(B_N^{(r)} - B_T^{(r)} \right) A^{(r)}, \tag{3.25}$$

where $\gamma = 1$ for fracture set 1 and $\gamma = 2$ for fracture set 2, so that $n_1^{(1)} = \cos\theta$, $n_3^{(1)} = -\sin\theta$ and $n_1^{(2)} = \cos\theta$, $n_3^{(2)} = \sin\theta$. It then follows from (3.22) and (3.23) that the non-vanishing components of α_{ij} and β_{ijkl} are α_{11}, α_{13}, α_{33}, β_{1111}, β_{1113}, $\beta_{1133} = \beta_{1313}$, β_{1333} and β_{3333}. These non-vanishing components may be written in the form

$$\alpha_{11} = (A_1 + A_2) \cos^2\theta, \tag{3.26}$$

$$\alpha_{13} = (A_2 - A_1) \cos\theta \sin\theta, \tag{3.27}$$

$$\alpha_{33} = (A_1 + A_2) \sin^2\theta, \tag{3.28}$$

$$\beta_{1111} = (B_1 + B_2) \cos^4\theta, \tag{3.29}$$

$$\beta_{1113} = (B_2 - B_1) \cos^3\theta \sin\theta, \tag{3.30}$$

$$\beta_{1133} = \beta_{1313} = (B_1 + B_2) \cos^2\theta \sin^2\theta, \tag{3.31}$$

$$\beta_{1333} = (B_2 - B_1) \cos\theta \sin^3\theta, \tag{3.32}$$

and

$$\beta_{3333} = (B_1 + B_2) \sin^4\theta. \tag{3.33}$$

For definitiveness, similarly to the case of a single fracture set, I assume that for each fracture set in the dry rock normal fracture compliance is equal to the tangential compliance, so that $B_1 = B_2 = 0$ and the fourth-rank tensor β_{ijkl} is identically zero. Substitution of

expressions (3.26)-(3.28) for α_{ij} and zero for β_{ijkl} into (2.2) yields the excess compliance tensor ΔS_{ijkl} due to the fractures and hence the compliance of the fractured medium, S_{ijkl} (2.1). The elastic stiffness tensor of the dry fractured medium is then obtained by calculating the inverse compliance tensor, S^{-1}_{ijkl}, and then transforming to the two-index 6×6 notation to obtain the stiffness matrix c^{dry}_{ij} of the dry fractured material. The saturated stiffness matrix c^{sat}_{ij} can now be computed using anisotropic Gassmann equations (2.5)-(2.9).

The phase velocities for vertically propagating shear-waves in the associated fluid-saturated medium are,

$$V_{S1} = \sqrt{\frac{\mu}{\rho}}, \tag{3.34}$$

and

$$V_{S2} = \sqrt{\frac{2}{\rho} \frac{c^{sat}_{33} c^{sat}_{55} - c^{sat2}_{35}}{c^{sat}_{33} + c^{sat}_{55} + \sqrt{\left(c^{sat}_{33} - c^{sat}_{55}\right)^2 + 4c^{sat2}_{35}}}}, \tag{3.35}$$

(see e.g., Helbig (1994)). The shear-wave splitting parameter can then be computed using definition (3.20). Figure 3-6 shows the splitting parameter as a function of the fluid modulus and fracture dip for $B_{T2}/B_{T1} = 1/2$. There is a weak dependence of splitting on K_f for this ratio of compliances and the sign reversal observed in Figure 3-5 is not present.

3.3.2 Non-interacting fracture sets

In the second scenario it is assumed that the two fracture sets (Figure 3-3) are in hydraulic interaction with the surrounding pores but not with each other, since they are separated into differing domains. Thus one can apply Gassmann equations independently to each fracture set to obtain effective saturated fracture compliances, which can then be substituted into the Sayers-Kachanov equations (2.1)-(2.4). First, note that the background medium in this approach is the fluid-saturated rock, whose bulk modulus is given

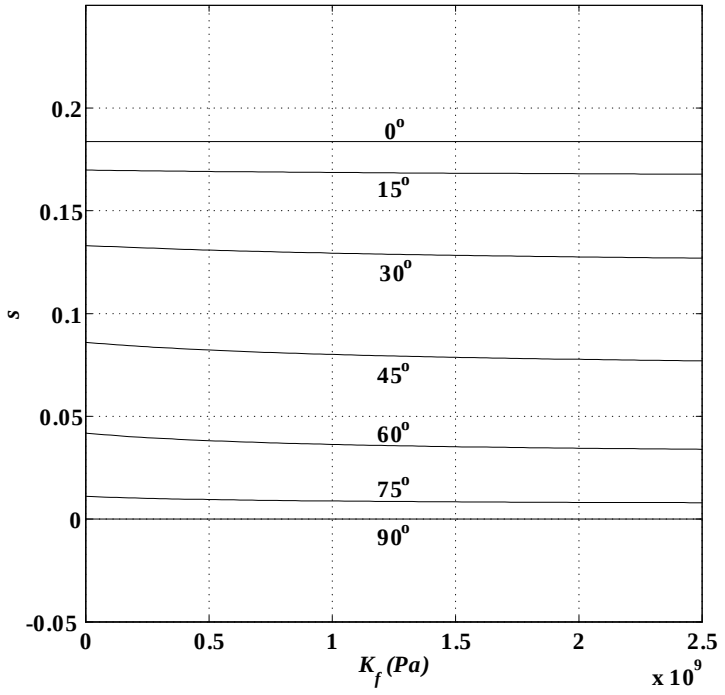

Figure 3-6: s vs K_f for the case of two conjugate fracture sets in full pressure equilibrium, $B_{T2}/B_{T1} = 1/2$ and $\theta = 0°$, $15°$, $30°$, $45°$, $60°$, $75°$ and $90°$: s is weakly dependent on K_f for this compliance ratio.

by the isotropic Gassmann equation,

$$K^{sat} = K + \frac{\alpha_0^2}{\frac{\alpha_0 - \phi}{K_g} + \frac{\phi}{K_f}}. \tag{3.36}$$

For each fracture set, the saturated fracture compliance can be obtained by inverting the stiffness matrix given by equations (2.5)-(2.9) to obtain the corresponding compliance matrix, then subtracting the compliance matrix for an isotropic saturated background rock with bulk and shear moduli K_{sat} and μ. This gives (Gurevich (2003)),

$$B_N^{sat} = B_N \frac{L^{sat}(\lambda+\mu)}{L\left(\lambda^{sat}+\mu\right)} \frac{1 - \frac{K_f}{K_g} + \frac{1}{3}\frac{K_f \mu \alpha_0}{\phi K_g (\lambda+\mu)}}{1 - \frac{K_f}{K_g} + \frac{K_f}{(1-\Delta_N)\phi K_g L}\left[\left(K_g + \frac{4}{3}\mu\right)\left(\alpha_0 + \frac{K^2}{K_g L}\Delta_N\right) - \frac{16}{9}\frac{\mu^2 \alpha_0}{L}\Delta_N\right]}, \tag{3.37}$$

where $\lambda^{sat} = K^{sat} - 2\mu/3$, $L^{sat} = \lambda^{sat} + 2\mu$, Δ_N is defined in (3.2), and μ is the shear modulus. Once the saturated excess compliances have been obtained for each of the two conjugate fracture sets, they can be substituted into equations (2.3) and (2.4) to obtain second and fourth rank tensors α_{ij} and β_{ijkl} (note that now equations (2.3) and (2.4) are used for the saturated rock, for which normal and tangential compliances are different, and therefore the fourth rank tensor β_{ijkl} is non-zero). The stiffness matrix of the saturated medium with two conjugate fracture sets can then be calculated by inverting the compliance tensor given by equations (2.1) and (2.2), where the background compliance tensor S^0_{ijkl} is again defined by the saturated moduli K^{sat} and μ. Figure 3-7 shows the splitting parameter as a function of the fluid modulus and fracture dip (always opposite and symmetrical) for $B_{T2}/B_{T1} = 1$. The splitting is dependent upon K_f in this case. Figure 3-8 shows the shear-wave splitting as a function of K_f for $B_{T2}/B_{T1} = 1/2$. Comparing with Figure 3-6, the dependency of splitting on K_f is much stronger here and a sign reversal similar to that present in Figure 3-5 can be seen. This case of incomplete pressure communication may not occur in the low-frequency limit, but may take place at finite frequency, as discussed in the next section.

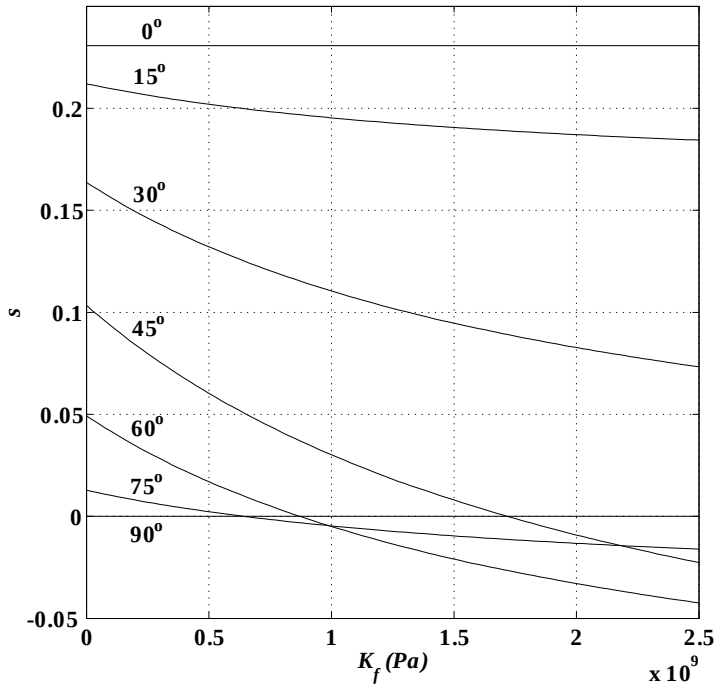

Figure 3-7: s vs K_f for the case of two conjugate fracture sets that are non-interacting, $B_{T2}/B_{T1} = 1$ and $\theta = 0°$, 15°, 30°, 45°, 60°, 75° and 90°. In this degenerate case of equal compliances, s is dependent on K_f.

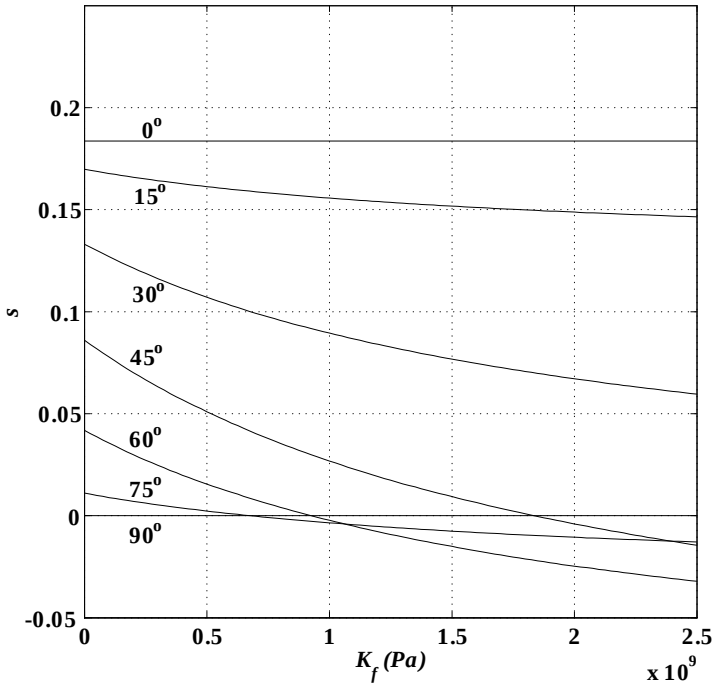

Figure 3-8: s vs K_f for the case of two conjugate fracture sets that are non-interacting, $B_{T2}/B_{T1} = 1/2$ and $\theta = 0°$, $15°$, $30°$, $45°$, $60°$, $75°$ and $90°$. s is dependent on K_f for this compliance ratio.

3.4 Discussion

As Figures 3-4 to 3-8 illustrate, the shear-wave splitting depends upon the elastic properties of the fluid filling the fractures except for the cases of wave propagation parallel or perpendicular to the plane of fracturing. This is because at the scale of the seismic wavelength the fractured medium is effectively anisotropic, therefore a pure shear-wave only exists when the elastic wave propagates along one of the symmetry axes. In any other direction the elastic wave is a quasi-shear mode. Hence a small amount of compressional deformation is taking place during passage of the wave and therefore the splitting is influenced by the fluid bulk modulus. The magnitude of this influence depends upon the frequency of the deformation, as is illustrated by the two alternative approaches for the case of conjugate fracture sets. In the first approach, the deformation is quasi-static, that is, it occurs slowly enough so that within the wave period there is enough time for the fluid to flow and equilibrate pressure throughout pores and both fracture sets. In this case Gassmann (1951) theory applies, and the magnitude of shear-wave splitting is controlled by the elastic symmetry of the dry matrix. In particular, when the two conjugate fracture sets have equal excess compliances, the medium is orthotropic, the vertical axis is a symmetry direction, and the vertically propagating shear-wave is again a pure shear-wave with no influence from the fluid.

In contrast, for some higher frequencies there may be enough time for pressure equilibration between fractures and surrounding pores, but not between the two fractures sets. More precisely, at finite frequency each fracture set may be in pressure equilibrium with the pore space in its immediate vicinity, but the pressure may not have time to equilibrate throughout the pore space. In that case the influence of each fracture set has to be considered separately. This situation is simulated by the second approach where each fracture set contributes to the fluid effect on the shear-wave splitting, resulting in a substantially larger splitting magnitude as shown in Figure 3-7.

Because of fracture intersections in Figure 3-2, this is only plausible for a fracture system of the type shown in Figure 3-3. This system has two characteristic wave propa-

gation frequencies (frequencies above which there is fluid flow and below which there is not) f_1 and f_2 which can be derived using a 1D analysis of the diffusion equation parallel to the normal to the fractures in a given domain as follows.

According to Biot's theory of poroelasticity, the equilibration of pressure p in a porous medium is governed by the diffusion equation (Biot (1962); Rice & Cleary (1976))

$$D\frac{\partial^2 p}{\partial x^2} = \frac{\partial p}{\partial t}, \tag{3.38}$$

where D is Biot's slow wave diffusivity given by

$$D = \frac{\kappa M\left(K + \frac{4}{3}\mu\right)}{\eta\left(K_{SAT} + \frac{4}{3}\mu\right)}, \tag{3.39}$$

$$M = \frac{\alpha_0 - \phi}{K_g} + \frac{\phi}{K_f}, \tag{3.40}$$

κ is the permeability, η is the dynamic viscosity of the fluid, and K_{SAT} is the undrained modulus of the saturated rock given by the Gassmann (1951) equation, $K_{SAT} = K + \alpha^2 M$. If the characteristic length scale in the problem is l_c, and the characteristic time $t_c = 1/f_c$ (where f_c is the characteristic frequency), then approximating both sides of equation (3.38) by finite differences we have

$$D\frac{\Delta p}{l_c^2} = \frac{\Delta p}{t_c}, \tag{3.41}$$

so that

$$t_c = \frac{l_c^2}{D}. \tag{3.42}$$

For $K_f \ll K, \mu$ equation (3.42) reduces to

$$f_c = \frac{\kappa K_f}{\eta\phi l_c^2}. \tag{3.43}$$

Taking $l_c = L$, the characteristic width of a domain of aligned fractures, gives

$$f_1 = \frac{\kappa K_f}{\eta \phi L^2}. \tag{3.44}$$

Taking $l_c = c/\phi$, the thickness of a layer within the porous medium having the same pore volume as the fracture (the porosity of the fracture is assumed to be unity) where c is the width of the fracture, gives

$$f_2 = \frac{\phi \kappa K_f}{\eta c^2}. \tag{3.45}$$

If $f \gg f_2$, the fractures appear isolated with respect to fluid flow. If $f_1 \ll f \ll f_2$, the fractures within a domain can be considered as being in pressure equilibrium with the surrounding medium, but not in equilibrium with fractures in neighboring domains. If $f \ll f_1$, the fractures are in pressure equilibrium with the pore space and with each other. Figure 3-9 plots f_1 and f_2, against matrix permeability, κ, for the case $c = 1mm$, $L = 10m$, $K_f = 2GPa$, $\eta = 0.001Pas$, and $\phi = 0.1$. The values of κ chosen are typical of low permeability reservoirs for which the fractures are essential to make production economic. It is seen that, for the parameters chosen, the critical frequency f_1 lies below the seismic band, implying that the fractures within a domain can be considered as being in equilibrium with the surrounding medium, but not in equilibrium with fractures in neighboring domains.

The preceding analysis is limited to two fixed frequency ranges: a low-frequency range where the first approach applies, and a higher frequency range where the second approach is more suitable. The effect of frequency has not been considered explicitly. An explicit analysis of the frequency dependency of shear-wave splitting would require use of dynamic models of wave propagation in porous fractured media (Hudson et al. (2001); Tod (2001); Chapman (2003); Maultzsch et al. (2003); Brajanovski et al. (2005) ; Galvin & Gurevich (2006)) and will be treated in the next two chapters.

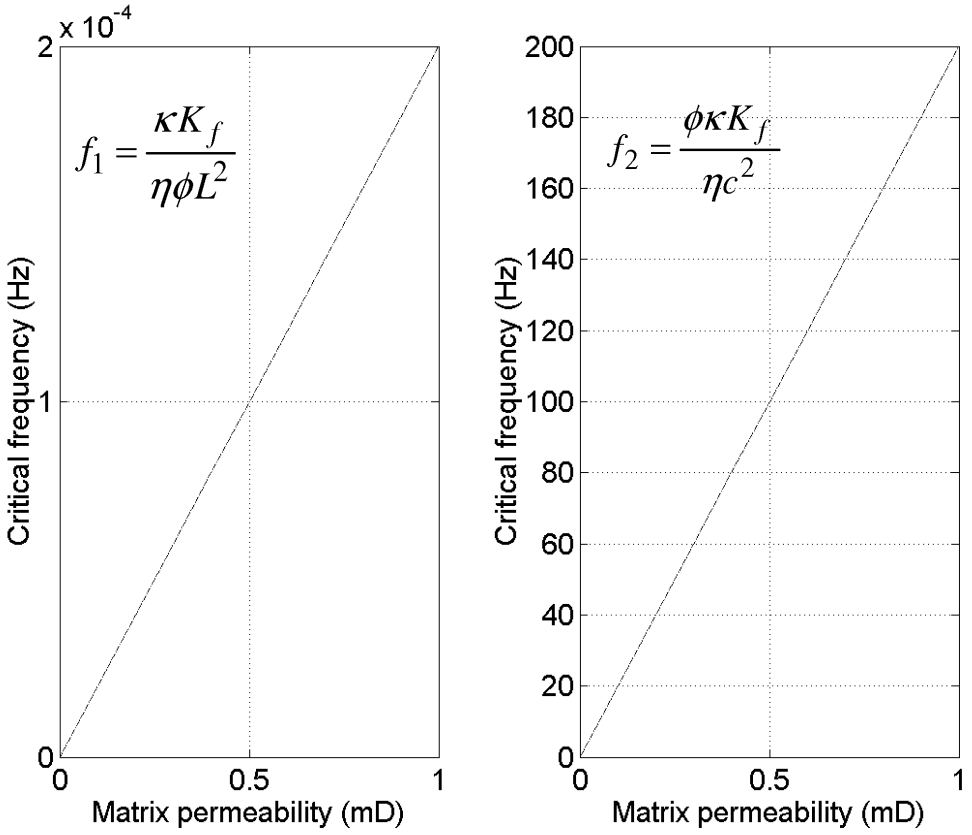

Figure 3-9: Plot of f_1 and f_2, against matrix permeability, κ, for the case $c = 1mm$, $L = 10m$, $K_f = 2GPa$, $\eta = 0.001Pas$, and $\phi = 0.1$. The values of κ chosen are typical of low permeability reservoirs for which the fractures are essential to make production economic.

Chapter 4

Scattering by a Single Crack in a Poroelastic Medium

4.1 Introduction

The description of the effects of fractures given in the previous chapter is applicable in the low-frequency limit, that is, when both the wavelength and the fluid diffusion length are much larger than the size of the pores and fractures. When we look at higher frequencies, we must take into account the actual finite geometry of the fractures in order to obtain effective medium properties. The simplest geometry that can be used to represent fracturing is the flat, circular (or "penny-shaped") crack. This crack geometry is effectively an oblate spheroid. The effect of a distribution of cracks on the passing wave can be estimated using multiple-scattering theory. This approach requires knowledge of the scattering that takes place due to the presence of a single crack, which is the subject of this chapter.

I consider the interaction of a plane longitudinal wave in a fluid-saturated porous medium with an open oblate spheroidal crack of radius a and small thickness $2c \ll a$ placed perpendicular to the direction of wave propagation. The background porous medium is assumed to be governed by Biot's equations of dynamic poroelasticity (Biot,

1962). This poroelastic problem is analogous to the problem of scattering by a crack in an elastic medium (Robertson (1967); Garbin & Knopoff (1973); Piau (1979)). In particular, Robertson (1967) formulated this problem in cylindrical co-ordinates as a system of dual integral equations in the Hankel transform of the wave field, which was then reduced to a Fredholm equation of the second kind. For fluid-saturated porous materials the interaction differs from that of the corresponding elastic scattering, as it involves flow of the pore fluid between the crack and the host medium, induced by the passing wave. This effect is particularly significant for thin cracks, as their high compliance (compared to that of the relatively stiff pores) causes the fluid to flow in and out of the crack during rarefaction and compression wave cycles. Recently, similar problems have been investigated in the fields of poroelasticity and the mathematically analogous thermoelasticity. Jin & Zhong (2002) investigated the dynamic stress intensity factor of a circular crack in an infinite poroelastic solid, however they only treated the case of impermeable crack surfaces. Sherief & El-Maghraby (2003) solve a dynamical problem for an infinite thermoelastic solid with an internal circular crack which is subjected to prescribed temperature and stress distributions. I apply a similar approach to the scattering by a crack in a porous medium.

I restrict the analysis to frequencies that are small compared to Biot's characteristic frequency. For typical porous materials such as reservoir rocks and soils this assumption is appropriate for frequencies of up to 10-100 kHz.

4.2 Problem Formulation

4.2.1 Equations of Poroelasticity

I consider an incident plane longitudinal wave, harmonic in time, propagating in a fluid-saturated porous medium in the positive direction of the z-axis of a cylindrical coordinate system. This wave can be represented as the displacement field $u_z^{(i)} = u_0 e^{ik_1 z}$, where k_1 is the wavenumber. I aim to derive the scattered field $\mathbf{u}(\mathbf{r})$ that results from interaction

between the incident wave and the crack, which occupies the circle $0 \leq r \leq a$ in the plane $z = 0$. The total displacement field is therefore $\mathbf{u}^{(t)}(\mathbf{r}) = u_z^{(i)}\mathbf{a}_z + \mathbf{u}(\mathbf{r})$, where $\mathbf{a}_z$ is a unit vector directed along the z-axis.

Since there exists geometrical symmetry about the crack plane $z = 0$, both the scattered and total displacement fields satisfy Biot's equations (as outlined in Chapter 2) in the semi-infinite poroelastic medium $z \geq 0$.

Because of the axial symmetry, there is no dependency upon the transverse angle θ. Using equations (2.27) and (2.28) one can therefore decompose equations (2.25) and (2.26) into scalar equations in cylindrical coordinates (r, θ, z):

$$\mu\left(\nabla^2 - \frac{1}{r^2}\right)u_r + (\lambda + \mu)\frac{\partial e}{\partial r} + \rho\omega^2 u_r - \alpha\frac{\partial p}{\partial r} = 0, \tag{4.1}$$

$$\mu\nabla^2 u_z + (\lambda + \mu)\frac{\partial e}{\partial z} + \rho\omega^2 u_z - \alpha\frac{\partial p}{\partial z} = 0, \tag{4.2}$$

$$\nabla^2 p + \frac{i\omega b}{M}p + i\alpha b\omega e = 0, \tag{4.3}$$

where $\lambda = K - 4\mu/3$, $b = \eta/\kappa$, and e is the cubical dilatation

$$e = \nabla \cdot \mathbf{u} = \frac{1}{r}\frac{\partial}{\partial r}(ru_r) + \frac{\partial u_z}{\partial z}. \tag{4.4}$$

Equations (4.1)-(4.3) are supplemented by the constitutive relations

$$\sigma_{zz} = 2\mu\frac{\partial u_z}{\partial z} + \lambda e - \alpha p, \tag{4.5}$$

$$\sigma_{rz} = \mu\left(\frac{\partial u_r}{\partial z} + \frac{\partial u_z}{\partial r}\right), \tag{4.6}$$

and using equation (2.26)

$$w_z = \frac{1}{i\omega b}\left(\frac{\partial p}{\partial z} - \rho_f\omega^2 u_z\right). \tag{4.7}$$

4.2.2 General Solution

Similarly to Sherief & El-Maghraby (2003) one can obtain the general solution of equations (4.1)-(4.3). I first obtain an equation containing p as its only unknown. Substituting equations (2.27) and (2.28) into equations (2.25) and (2.26) and combining them in the low frequency limit I arrive at the equation

$$\left(L\nabla^2 + \rho\omega^2\right) e - \alpha\nabla^2 p = 0, \tag{4.8}$$

where $L = \lambda + 2\mu$. Eliminating e from equations (4.3) and (4.8) results in

$$\left[\nabla^4 + \left(k_1^2 + k_2^2\right)\nabla^2 + k_1^2 k_2^2\right] p = 0, \tag{4.9}$$

where $k_0 = \sqrt{\rho\omega^2/L}$, $k_1 = \sqrt{\rho\omega^2/H}$ is the wavenumber of the fast compressional wave and $k_2 = \sqrt{i\omega bH/LM}$ is the wavenumber of the slow compressional wave. In this low frequency limit of Biot's equations the wavelength of the slow compressional wave is small compared to that of the fast compressional wave,

$$k_1 \ll |k_2| . \tag{4.10}$$

Factorising equation (4.9) into the form

$$\left(\nabla^2 + k_1^2\right)\left(\nabla^2 + k_2^2\right) p = 0 \tag{4.11}$$

allows one to write the solution of equation (4.9) in the form $p = p_1 + p_2$ where p_i is the solution of the equation

$$\left(\nabla^2 + k_i^2\right) p_i = 0 \qquad i = 1, 2. \tag{4.12}$$

In order to obtain the solution p one must reduce the partial differential equation (4.12) to an ordinary one. I can do this by applying the Hankel transform with respect to the

radial coordinate r:

$$f^*(y,z) = \mathcal{H}[f(r,z)] = \int_0^\infty f(r,z)\, r J_0(yr)\, dr, \tag{4.13}$$

where J_0 is the Bessel function of the first kind of order zero and y is a radial wavenumber. The inverse Hankel transform is given by

$$f(r,z) = \mathcal{H}^{-1}[f^*(y,z)] = \int_0^\infty f^*(y,z)\, y J_0(yr)\, dy. \tag{4.14}$$

Taking the Hankel transform of equation (4.12) and using the operational relationship

$$\mathcal{H}\left(\frac{\partial^2 f(r,z)}{\partial r^2} + \frac{1}{r}\frac{\partial f(r,z)}{\partial r}\right) = -y^2 f^*(y,z) \tag{4.15}$$

I obtain the ordinary differential equation

$$\left(\frac{\partial^2}{\partial z^2} + k_i^2 - y^2\right) p_i^* = 0 \qquad i = 1, 2. \tag{4.16}$$

Due to the symmetrical nature of the problem, the solution to equation (4.16) can be written as

$$p = \int_0^\infty \left[\sum_{i=1}^{2} A_i(y)\left(k_0^2 - k_i^2\right) e^{-q_i z}\right] y J_0(yr)\, dy \tag{4.17}$$

where $q_i = \sqrt{y^2 - k_i^2}$ (so that $iq_i = \sqrt{k_i^2 - y^2}$ is the axial wavenumber). I can now obtain all other field variables using solution (4.17) and the governing and constitutive relations. An equation for e can be obtained by applying the Hankel transform to equation (4.8) and substituting (4.17):

$$e = -\frac{\alpha}{L}\int_0^\infty \left[\sum_{i=1}^{2} A_i(y)\, k_i^2 e^{-q_i z}\right] y J_0(yr)\, dy. \tag{4.18}$$

The expression for u_z is obtained from equation (4.2) using solutions (4.17) and (4.18):

$$u_z = \int_0^\infty \left[A_3(y)\, e^{-q_3 z} - \frac{\alpha}{L} \sum_{i=1}^{2} A_i(y)\, q_i e^{-q_i z} \right] y J_0(yr)\, dy. \tag{4.19}$$

In similar fashion, making use of the Bessel function identity

$$x J_n'(x) \pm n J_n(x) = \pm x J_{n\mp 1}(x) \tag{4.20}$$

I obtain an expression for u_r:

$$u_r = \int_0^\infty \left[A_3(y)\, q_3 e^{-q_3 z} - \frac{\alpha y^2}{L} \sum_{i=1}^{2} A_i(y)\, e^{-q_i z} \right] J_1(yr)\, dy \tag{4.21}$$

where J_1 is the Bessel function of the first kind of order one. Substituting equations (4.17), (4.18), (4.19) and (4.21) into constitutive relations (4.5) and (4.6) and using identity (4.20) I obtain the components of the stress tensor:

$$\sigma_{zz} = \mu \int_0^\infty \left[\frac{\alpha\,(2y^2 - k_3^2)}{L} \sum_{i=1}^{2} A_i(y)\, e^{-q_i z} - 2A_3(y)\, q_3 e^{-q_3 z} \right] y J_0(yr)\, dy \tag{4.22}$$

and

$$\sigma_{rz} = \mu \int_0^\infty \left[\frac{2y^2 \alpha}{L} \sum_{i=1}^{2} A_i(y)\, q_i e^{-q_i z} - A_3(y) \left(2y^2 - k_3^2\right) e^{-q_3 z} \right] J_1(yr)\, dy. \tag{4.23}$$

Equations (4.17)-(4.23) give the complete solution of the scattering problem in terms of the three scalar spectral amplitude functions $A_1(y)$, $A_2(y)$, and $A_3(y)$. In order to find the unknown $A_i(y)$, $i = 1, 2, 3$, one must derive the boundary conditions that are valid for this problem at $z = 0$.

4.2.3 Boundary Conditions

I assume that the circular crack is in hydraulic communication with the surrounding porous medium. The general boundary conditions for an interface between a porous medium and a porous inclusion are well known (Deresiewicz & Skalak, 1963). These conditions, written in cylindrical co-ordinates for the special case of a fluid-filled crack, are:

(i) continuity of total normal stress

$$\sigma_{zz} = -p' \tag{4.24}$$

(ii) continuity of total tangential stress

$$\sigma_{rz} = 0 \tag{4.25}$$

(iii) continuity of fluid pressure

$$p = p' \tag{4.26}$$

(iv) continuity of the normal component of the fluid displacement

$$(1 - \phi)u_z + \phi U_z = U'_z \tag{4.27}$$

where the primed quantities refer to the free fluid in the crack.

Due to the planar symmetry of the problem I only need to obtain the boundary conditions that are applied at the surface $z = 0$ of the semi-infinite porous medium $z \geqslant 0$. Here and below I neglect the compressibility of the fluid in the crack (but not in the pores!). As shown in Hudson (1981), this assumption is valid when the change in volume of the crack-filling fluid is negligibly small, which in turn requires that

$$\frac{K_f}{\mu} \gg \frac{c}{a}, \tag{4.28}$$

where as before K_f is the bulk modulus of the fluid in the crack, μ is the shear modulus of the background medium, and c/a is the aspect ratio of the crack. Note that in an elastic medium a crack filled with an incompressible fluid does not cause any scattering of a normally incident P-wave. Analogously, in a porous medium such a crack will not cause any scattering of a normally incident P-wave at frequencies where the size of the crack a is comparable to the wavelength of the incident wave. However, there may still be scattering of incident energy due to fluid flow between the crack and the pore space. As will be seen, this effect occurs at much lower frequencies where the crack radius is comparable to the wavelength of Biot's slow wave.

For an incompressible fluid in the crack, the volume-fraction-average of the normal displacement $(1-\phi)u_z + \phi U_z = u_z + w_z$ at the face of the crack must be equal to zero. Boundary condition (4.24) tells me that both $\sigma_{zz}^{(t)}$ and $p^{(t)}$ in the *total* field at $z = 0^+$ must be equal to the pressure of the crack-filling fluid, $p^{(c)}$, so that $\sigma_{zz}^{(t)} = p^{(t)}$ or $\sigma_{zz} - p = -(\sigma_{zz}^{(i)} - p^{(i)})$. Also, analogously to the elastic case, σ_{rz} is everywhere zero, and $u_z = w_z = 0$ due to symmetry considerations. Expressing stress and fluid pressure in terms of displacement via constitutive relations (4.5) and (2.28) the boundary conditions can be written:

$$\sigma_{rz} = 0 \qquad 0 \le r < \infty, \tag{4.29}$$

$$u_z = 0 \qquad a < r < \infty, \tag{4.30}$$

$$w_z = 0 \qquad a < r < \infty, \tag{4.31}$$

$$u_z + w_z = 0 \qquad 0 \le r \le a, \tag{4.32}$$

and

$$\sigma_{zz} + p = -ik_1(H - \alpha M)u_0 \qquad 0 \le r \le a, \tag{4.33}$$

where it is noted that conditions (4.30)-(4.32) can be combined to give the single condition

$$u_z + w_z = 0 \qquad 0 \le r \le \infty. \tag{4.34}$$

Equations (4.17)-(4.23) together with boundary conditions (4.29)-(4.33) provide a complete formulation of the scattering problem.

4.3 Method of solution

The first step is to express two of the three unknown $A_i(y)$ in terms of the third, say, $A_1(y)$. Substituting equation (4.23) into condition (4.29) gives me the relation

$$A_3(y) = \frac{2y^2\alpha}{L(2y^2 - k_3^2)} \sum_{i=1}^{2} A_i(y) q_i. \tag{4.35}$$

Using condition (4.34) and equations (4.7) and (4.35) I obtain for $A_2(y)$:

$$A_2(y) = -\frac{q_1}{q_2 k_2^2 L} \frac{2y^2 L(k_1^2 - k_0^2) + i\alpha b\omega k_3^2}{2y^2 - k_3^2(1 - \frac{\alpha M}{H})} A_1(y). \tag{4.36}$$

I can now substitute equations (4.19), (4.22) and (4.17) into the remaining boundary conditions (4.30) and (4.33) and use relations (4.35) and (4.36) to obtain a pair of dual integral equations in the unknown function $A_1(y)$:

$$\int_0^\infty [F_1(y) - F_2(y)] A_1(y) y J_0(yr)\, dy = -ik_1(H - \alpha M)u_0 \qquad 0 \le r \le a, \tag{4.37}$$

$$\frac{\alpha k_3^2}{L} \int_0^\infty \frac{q_1}{2y^2 - k_3^2(1 - \frac{\alpha M}{H})} A_1(y) y J_0(yr)\, dy = 0 \qquad a < r < \infty, \tag{4.38}$$

where

$$F_1(y) = \frac{\alpha g \left[(2y^2 - k_3^2)^2 - 4y^2 q_1 q_3\right] + (2y^2 - k_3^2)(k_0^2 - k_1^2)}{2y^2 - k_3^2}, \tag{4.39}$$

$$F_2(y) = \frac{q_1}{q_2} \frac{[2y^2 L(k_1^2 - k_0^2) + i\alpha b\omega k_3^2][4\alpha g y^2(y^2 - q_2 q_3) - k_2^2(2y^2 - k_3^2)]}{k_2^2 L(2y^2 - k_3^2)\left[2y^2 - k_3^2(1 - \frac{\alpha M}{H})\right]}, \tag{4.40}$$

and $g = \mu/L$. Dual integral equations (4.37) and (4.38) can be reduced to the form discussed by Noble (1963) by substituting for a new unknown $B(y)$, related to $A_1(y)$

through the equation

$$B(y) = -\frac{2\alpha\mu(1-g)k_3^2 q_1 y}{L\left[2y^2 - k_3^2(1-\frac{\alpha M}{H})\right]} A_1(y). \tag{4.41}$$

This substitution yields

$$\int_0^\infty y\left[1+T(y)\right] B(y) J_0\left(yr\right) dy = -p_0 \qquad 0 \le r \le a, \tag{4.42}$$

$$\int_0^\infty B(y) J_0\left(yr\right) dy = 0 \qquad a < r < \infty, \tag{4.43}$$

where

$$T(y) = \left[1 + \frac{\alpha M k_3^2}{H\left(2y^2 - k_3^2\right)}\right]\left[T_1(y) - T_2(y)\right] - 1, \tag{4.44}$$

$$T_1(y) = \frac{M(k_2^2 L - 2\alpha\mu y^2)\left[4\alpha g y^2(y^2 - q_2 q_3) - k_2^2\left(2y^2 - k_3^2\right)\right]}{2\mu H(1-g)k_2^2 q_2 y\left[2y^2 - k_3^2(1-\frac{\alpha M}{H})\right]}, \tag{4.45}$$

$$T_2(y) = \frac{\alpha g\left[\left(2y^2 - k_3^2\right)^2 - 4y^2 q_1 q_3\right] + \left(2y^2 - k_3^2\right)\left(k_0^2 - k_1^2\right)}{2\alpha g(1-g)k_3^2 q_1 y}, \tag{4.46}$$

and $p_0 = ik_1(H - \alpha M)u_0$. Note that the factor $-2\mu(1-g)$ was included in definition (4.41) to ensure that

$$\lim_{y\to\infty} T(y) = 0, \tag{4.47}$$

which is required in order to follow Noble's solution method.

As shown in Chapter 2, a pair of dual integral equations (4.42) and (4.43) with

$$\lim_{y\to\infty} T(y) = 0 \tag{4.48}$$

are equivalent to a single Fredholm equation of the second kind

$$\theta(z) + \frac{1}{\pi}\int_0^a M(z,\xi)\theta(\xi)d\xi = -p_0 z, \tag{4.49}$$

where

$$M(z,\xi) = \pi(z\xi)^{\frac{1}{2}} \int_0^\infty yT(y) J_{\frac{1}{2}}(zy) J_{\frac{1}{2}}(\xi y) dy, \tag{4.50}$$

and

$$B(y) = \frac{2}{\pi} \int_0^a \theta(\xi) \sin(\xi y) d\xi. \tag{4.51}$$

I now manipulate these equations in order to express the Fredholm equation directly in terms of B. Substituting for the Bessel functions in equation (4.50) using the relationship

$$J_{\frac{1}{2}}(x) = \sqrt{\frac{2}{\pi x}} \sin x, \tag{4.52}$$

changing the order of integration in equation (4.49) and then using equation (4.51) I obtain

$$\theta(z) + \int_0^\infty T(y) \sin(zy) B(y) dy = -p_0 z. \tag{4.53}$$

I then multiply (4.53) through by $(2/\pi)\sin(xz)$ and integrate from 0 to a with respect to z. Changing the order of integration to evaluate $\int_0^a \sin(zy)\sin(zx)dx$ and then evaluating the RHS using integration by parts yields:

$$B(x) + \frac{1}{\pi} \int_0^\infty R(x,y) T(y) B(y) dy = -p_0 S(x), \tag{4.54}$$

where

$$R(x,y) = \frac{\sin a(x-y)}{x-y} - \frac{\sin a(x+y)}{x+y} \tag{4.55}$$

and

$$S(x) = \frac{2}{\pi} \frac{\sin ax - ax \cos ax}{x^2}. \tag{4.56}$$

Since an analytical solution to equation (4.54) exists only when its kernal function $R(x,y)T(y)$ is separable, in general one must obtain $B(y)$ via numerical methods.

4.4 Discussion

I obtain $B(y)$ numerically using the method of quadratures. Having obtained $B(y)$ one can calculate any field quantity of interest using the relationships given in the previous sections. Of particular interest are the scattering cross-section and the displacement of fluid relative to the solid, $\mathbf{w}$, as it represents the fundamental difference between elasticity and poroelasticity.

The scattering cross-section is a measure of the proportion of incident energy that becomes scattered. Analogously to the elastic case (see Robertson (1967)) the scattering cross-section Σ_p for a normally-incident longitudinal wave is given by

$$\Sigma_p = \frac{4\pi}{k_1} \operatorname{Im} g(0,0), \tag{4.57}$$

where $g(0,0)$ is the far-field amplitude of the scattered longitudinal wave in the direction of the incident wave. As in Robertson (1967) I can determine $g(0,0)$ by considering the far-field asymptotics of equation (4.19):

$$g(0,0) = \frac{i\alpha k_1 q_1}{L} A_1(0). \tag{4.58}$$

Figure 4-1 shows the scattering cross section as a function of dimensionless frequency, taking its maximum value around the dimensionless frequency $|k_2 a|^2 = 1$.

Figures 4-2 and 4-3 show the spectral amplitudes of the components of $\mathbf{w}$ at $z = 0$ as functions of normalised horizontal slowness $y/|k_2|$ plotted for a range of dimensionless frequencies. For frequencies such that the crack is small compared to the wavelength, w_z is distributed uniformly amongst the radial wavenumbers. As frequencies increase, however, the dominant radial wavenumbers are those closer to zero. w_z achieves it's maximum value around the frequency $|k_2 a|^2 = 1$. w_r decreases with increasing frequency.

In the next chapter I will use the single scattering result derived here to estimate the effective properties of a medium containing a distribution of cracks.

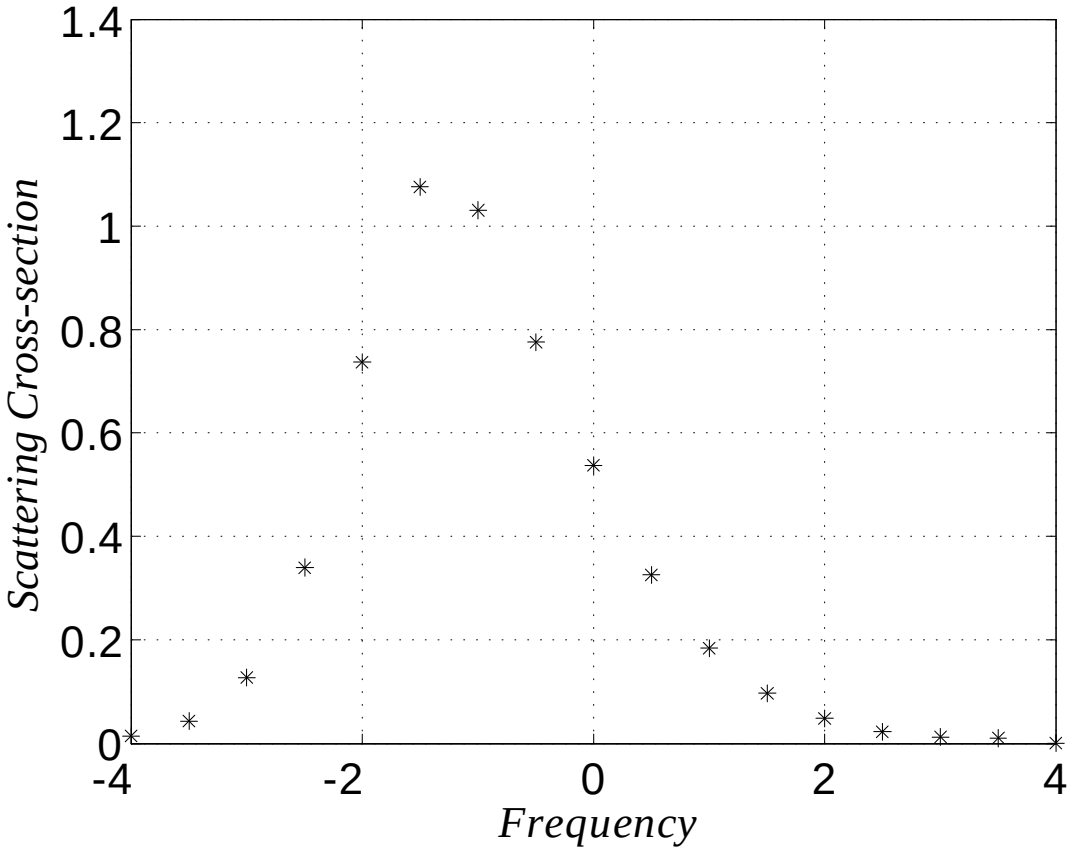

Figure 4-1: Scattering cross-section as a function of dimensionless frequency.

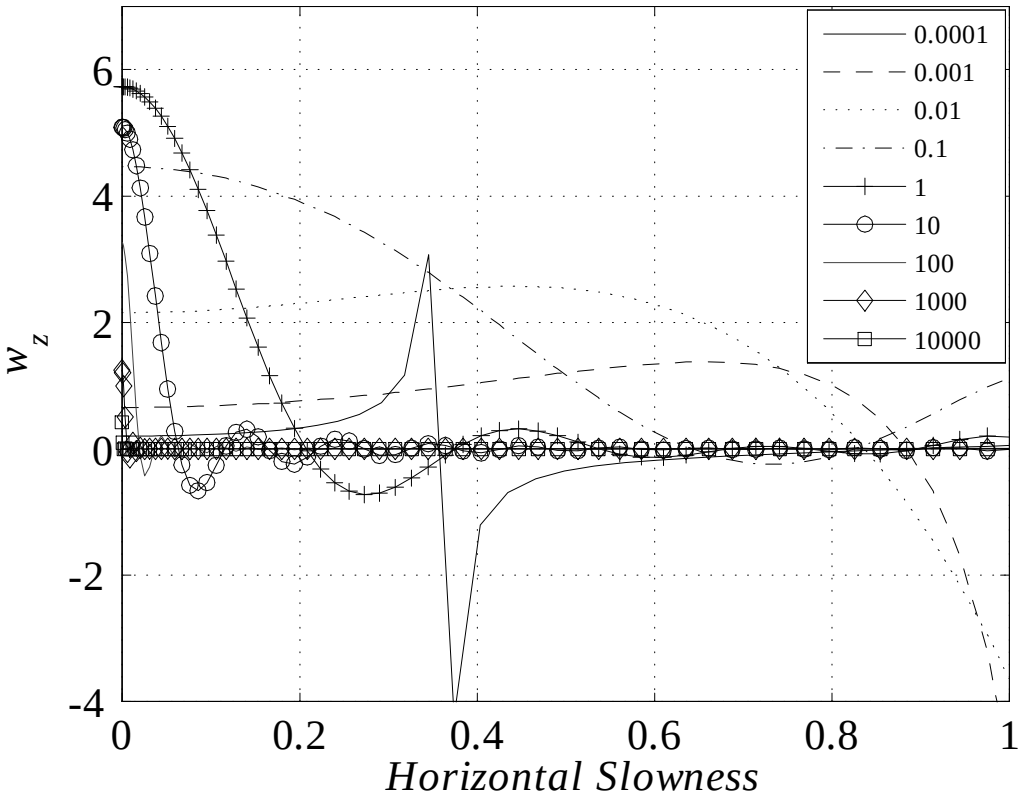

Figure 4-2: Vertical relative fluid displacement w_z vs normalised horizontal slowness $y/|k_2|$ for a range of dimensionless frequencies.

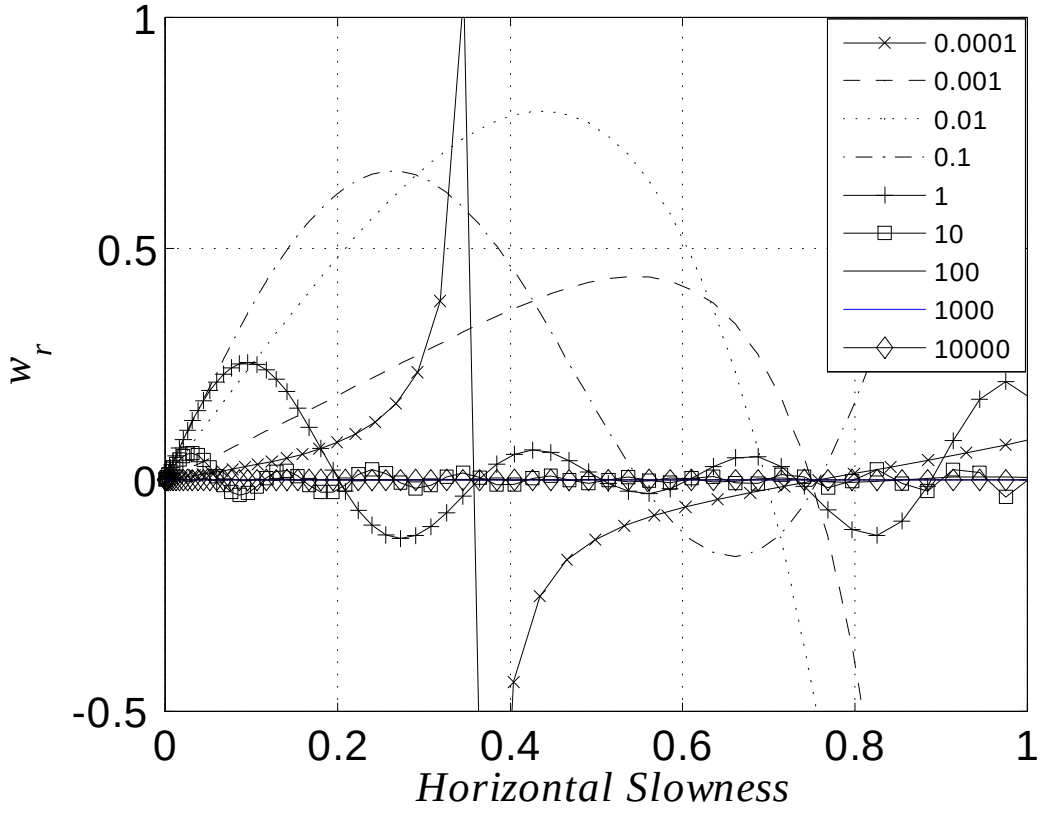

Figure 4-3: Radial relative fluid displacement w_r vs normalised horizontal slowness $y/|k_2|$ for a range of dimensionless frequencies.

Chapter 5

Effective Properties of a Poroelastic Medium Containing a Distribution of Aligned Cracks

5.1 Introduction

In Chapter 4 I derived the scattering by a single crack in a poroelastic medium. I can now use this single scattering result to estimate the effective properties of a medium containing a distribution of cracks. As mentioned in the Introduction, a number of schemes tackling this dynamic problem in fractured porous rocks are currently available. Brajanovski et al. (2005) model a fractured medium as very thin, highly porous layers in a porous background. Their model implies that these fractures are of infinite extent and therefore is valid when fracture spacing is much smaller than fracture length (diameter). The case of finite-size fractures was considered by Hudson et al. (1996), who model fractures as thin penny-shaped voids, and account for fluid flow effects by applying the diffusion equation to a single crack and ignoring interaction between cracks. This approximation however leads to some unphysical effects, such as the result that the anisotropy of the fluid-saturated fractured and porous rock in the low frequency limit is the same

as for the dry rock (Hudson et al. (2001); Chapman (2003); Brown & Gurevich (2004)).

Chapman (2003) and Maultzsch et al. (2003) analyse frequency-dependent anisotropy caused by the presence of meso-scale fractures in a porous rock, by considering connectivity of individual fractures, pores and microcracks. A more general computational model which can take account of pores and fractures of any size and shape was proposed by Jakobsen et al. (2003) using the T-matrix approximation, commonly used to study effective properties of heterogeneous media. In the T-matrix approximation the effect of voids (pores, fractures) is introduced as a perturbation of the solution for the elastic background medium.

The approach presented in this chapter is to model the effect of fractures as a perturbation with respect to an isotropic porous background medium. This approach seems attractive because it allows one to use all the machinery of the theory of wave propagation in fluid-saturated porous media, (Biot, 1962), without specifying individual shapes of grains or pores. It also seems logical to assume that the perturbation of the porous medium caused by the introduction of fractures will be much smaller than the perturbation caused by putting all the pores and fractures into an elastic solid.

In this chapter I simulate the effect of fractures by considering them to be thin circular cracks in a poroelastic background. I assume that the cracks are mesoscopic (large compared to the pore size, but small compared to the fast wave wavelength). Using the solution of the scattering problem for a single crack obtained in Chapter 4 and the multiple-scattering theory of Waterman & Truell (1961) (outlined in Chapter 2) I estimate the attenuation and dispersion of elastic waves taking place in a porous medium containing a sparse distribution of such cracks (Figure 5-1).

5.2 A Sparse Distribution of Cracks

The multiple scattering expressions (2.23) and (2.24) allow one to model the dispersion and attenuation due to the scattering of a plane elastic wave by cracks randomly dis-

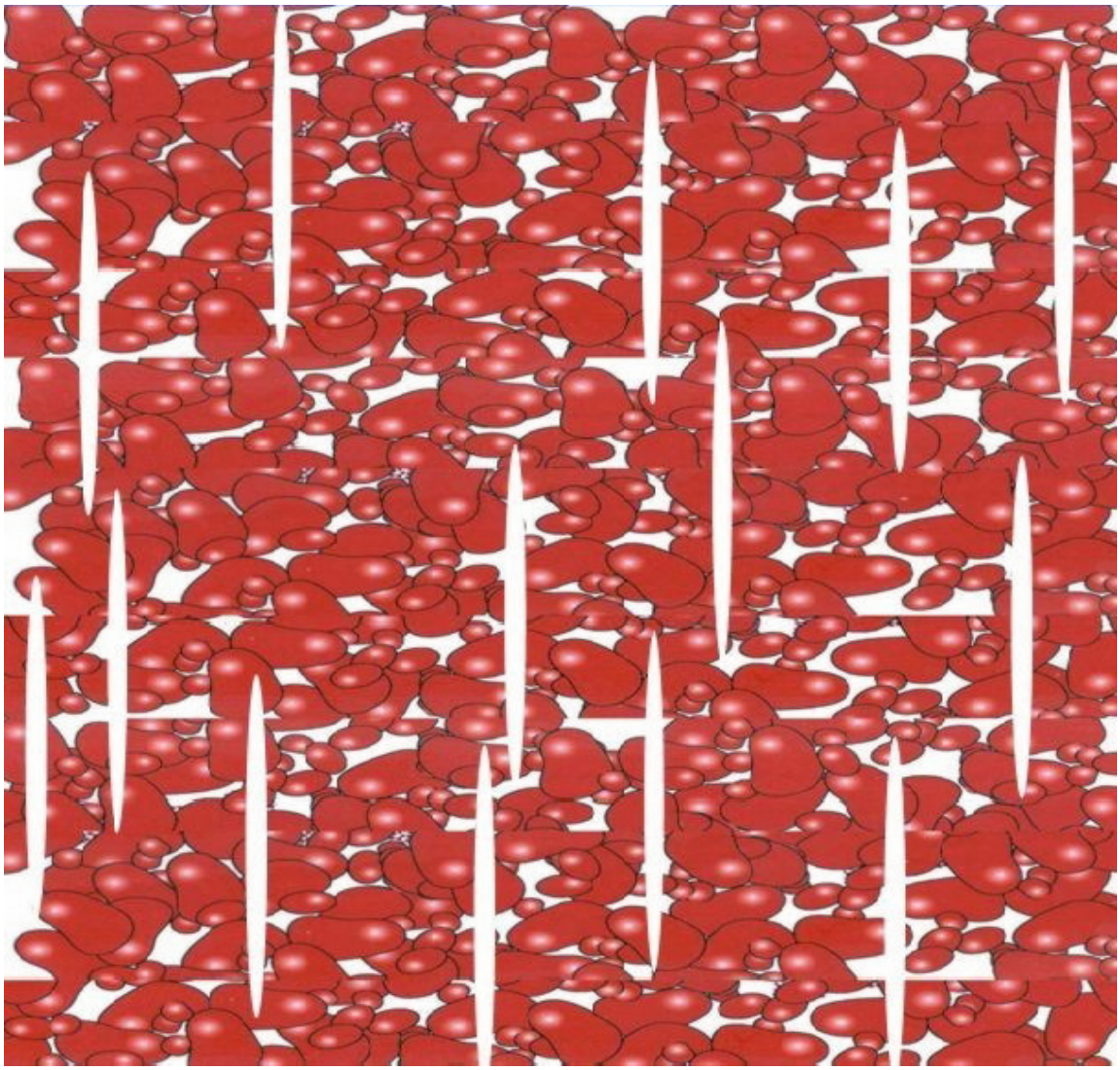

Figure 5-1: A porous medium containing a sparse distribution of cracks.

tributed throughout a poroelastic medium. I investigate the special case of dispersion and attenuation due to aligned cracks using the solution for the scattering by a circular crack derived in the previous section. My $f(0)$ is obtained analogously to the elastic case (Robertson, 1967) by considering the far-field asymptotics of

$$u_z = \int_0^\infty \left[A_3(y)\, e^{-q_3 z} - \frac{\alpha}{L} \sum_{i=1}^{2} A_i(y)\, q_i e^{-q_i z} \right] y J_0(yr)\, dy, \tag{5.1}$$

where the $A_i(y)$ are the spectral amplitudes of the fast, slow and shear waves for a single crack as discussed in Chapter 4, and is given by

$$f(0) = \frac{i\alpha k_1 q_1}{L} A_1(0) = -\frac{ik_1}{u_0} \frac{(H - \alpha M)}{2\mu H(1-g)} \lim_{y \to 0} \frac{B(y)}{y}. \tag{5.2}$$

5.3 Results

5.3.1 Numerical solution

The solution for intermediate frequencies was obtained numerically by the method of quadratures. Figures 5-2 and 5-3 show this solution in terms of effective velocity $v(\omega) = \omega / \operatorname{Re} k^*$ (normalized) and dimensionless attenuation $Q^{-1} = 2 \operatorname{Re} k^* / \operatorname{Im} k^*$ as functions of dimensionless frequency. Also shown in Figure 5-3 are asymptotic solutions in the low- and high-frequency limits (explained in the following sections), the equant porosity model of Hudson et al. (1996), and the result for spherical inclusions (Ciz et al., 2006) for comparison. The solution exhibits a typical relaxation peak around a normalized frequency ω' of about 10, or at circular frequency $f = \omega/2\pi \simeq 2\kappa M(K + 4\mu/3)/H\eta a^2$, the frequency where the fluid diffusion length $1/|k_2|$ is of the order of the crack radius a

.

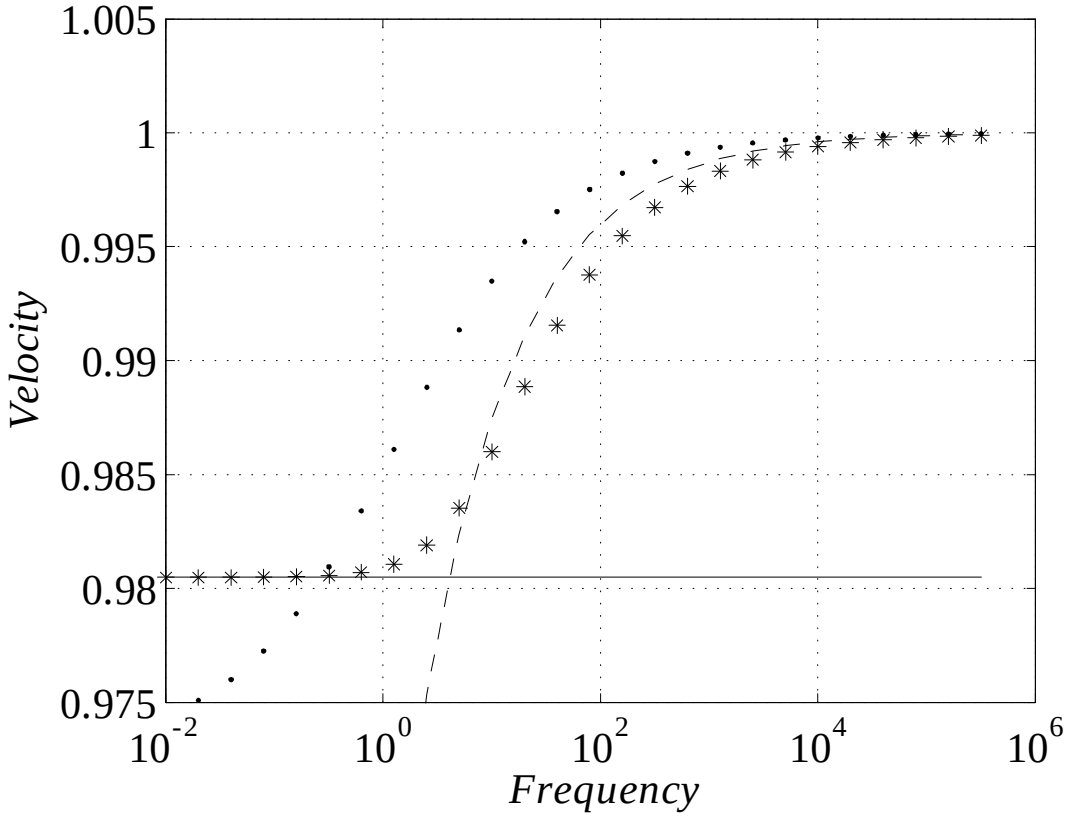

Figure 5-2: Dimensionless velocity as a function of dimensionless frequency: numerical solution (asterisks), low-frequency asymptotic (solid line), high-frequency asymptotic (dashed line) and the Hudson et al. (1996) equant porosity model (dots).

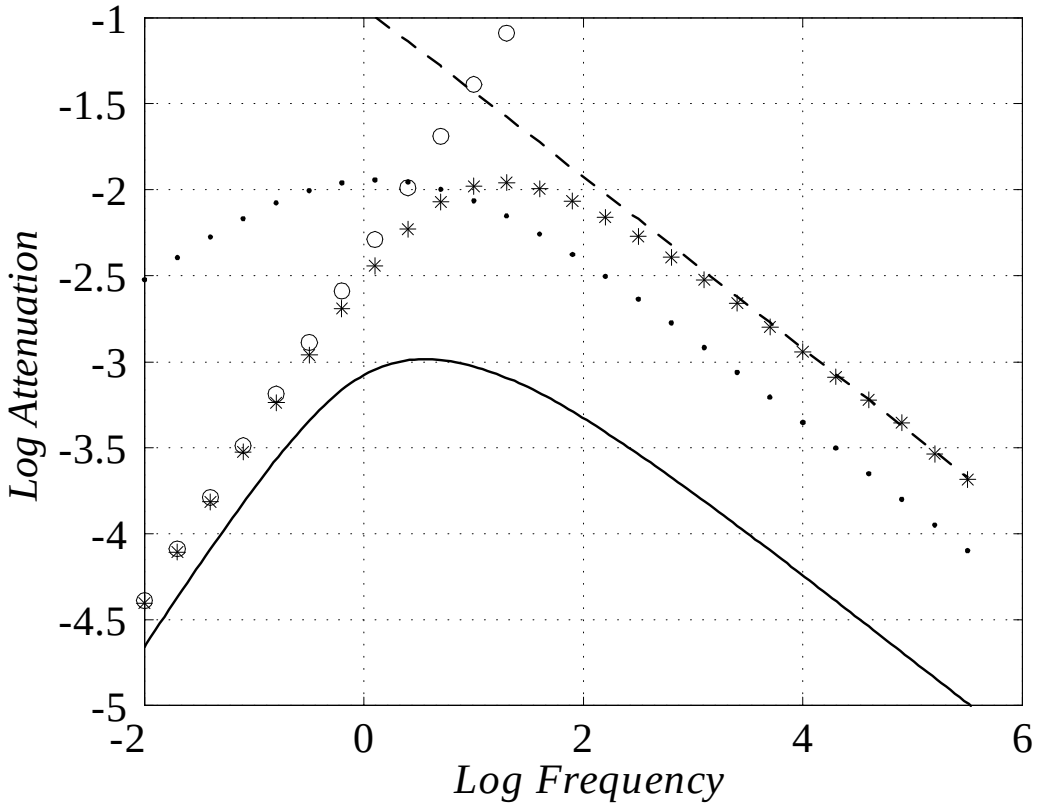

Figure 5-3: Dimensionless attenuation as a function of dimensionless frequency: numerical solution (asterisks), low-frequency asymptotic (circles), high-frequency asymptotic (dashed line), the Hudson et al. (1996) equant porosity model (dots) and the result for spherical inclusions (solid line).

5.3.2 Analytical solution

Mesoscopic cracks

The kernel function $T(y)$ (derived in Chapter 4, see equation 4.44) is general with regards to the size of the crack relative to the incident wavelength. However we are mainly interested in situations where the scattering is due to wave-induced fluid flow to and from the cracks (ie. the slow wave). For the scattering to be predominantly due to fluid flow, the crack size must be small relative to the wavelength of the incident compressional wave, $k_1 a \ll 1$ (mesoscopic cracks), so that scattering into the slow wave mode is dominant. For significant slow wave scattering to take place the radial wavenumber y should be of the order of $1/a$, or in other words $y \gg k_1$ and I can approximate expression (4.44) as

$$T(y) \approx M \frac{(2\alpha g y^2 - k_2^2)^2 - 2yq_2\alpha g\left[k_2^2(\alpha g - 2) + 2\alpha y^2 g\right]}{2Hg(g-1)yq_2k_2^2}. \tag{5.3}$$

I now obtain asymptotic solutions in the low and high frequency limits. Note that we are still in the low frequency regime of Biot theory, the low and high frequency limits I evaluate here are with respect to the extent to which fluid is able to diffuse between crack and pore space during passage of the wave field. That is, in the low frequency limit there is plenty of time available for fluid flow to occur, the diffusion length can be taken large compared with the crack radius, or $|k_2|\, a \ll 1$. At increasingly high frequencies there is no time available for appreciable fluid flow to occur and therefore the diffusion length can be taken as small compared with the crack radius, $|k_2|\, a \gg 1$.

Low frequency asymptote

For low frequencies $|k_2|\, a \ll 1$. Then $S(y)$ only contributes significantly to the integral in equation (4.54) for y of the order $1/a$. For $y \ll 1/a$, $S(y)$ is small. Thus $T(y)$ only contributes to the integral in (4.54) for $y \gg |k_2|$. In this case (5.3) can be simplified to give

$$T_{low}(y) \approx \frac{-Mk_2^2(2L^2 + 3\alpha^2\mu^2 - 4\alpha\mu L)}{4H\mu(L-\mu)y^2}. \tag{5.4}$$

At low frequencies the contribution of the integral in (4.54) is small relative to the RHS and therefore equation (4.54) can be solved by iteration . That is, assuming an initial solution $B(x) = -p_0 S(x)$ and then substituting $B(y) = -p_0 S(y)$ and $T(y) \approx T_{low}(y)$ into (4.54), yields

$$B(x) = -p_0 S(x) + \frac{p_0}{\pi} \int_0^\infty R(x,y) T(y) S(y) dy. \tag{5.5}$$

Because I actually require the limit of $B(x)/x$ as $x \to 0$ I can simplify the integral in equation (5.5) by rewriting it

$$\lim_{x\to 0} \frac{B(x)}{x} = -p_0 \lim_{x\to 0} \frac{S(x)}{x} + \frac{p_0}{\pi} \int_0^\infty \lim_{x\to 0} \frac{R(x,y)}{x} T(y) S(y) dy \tag{5.6}$$

and then evaluating the limits on the RHS. Expanding $R(x,y)/x$ using the trigonometric identity

$$\sin(A \pm B) = \sin A \cos B \pm \cos A \sin B, \tag{5.7}$$

I obtain

$$\frac{R(x,y)}{x} = \frac{2\left(y \sin ax \cos ay - x \cos ax \sin ay\right)}{x(x^2 - y^2)}. \tag{5.8}$$

As $x \to 0$, $\sin ax \approx ax$ and $\cos ax \approx 1$ so that equation (5.8) simplifies to

$$\frac{R(x,y)}{x} \approx \frac{2\left(\sin ay - ay \cos ay\right)}{y^2} = \pi S(y). \tag{5.9}$$

At small x,

$$\sin ax - ax \cos ax \approx \frac{(ax)^3}{3} \tag{5.10}$$

and hence

$$\frac{S(x)}{x} \approx \frac{2a^3}{3\pi}. \tag{5.11}$$

Therefore equation (5.6) simplifies to

$$\lim_{x\to 0}\frac{B(x)}{x} = -\frac{2p_0a^3}{3\pi} + p_0\int_0^\infty T_{low}(y)[S(y)]^2dy \tag{5.12}$$

which, upon evaluation of the integral, yields

$$\lim_{x\to 0}\frac{B(x)}{x} = \frac{p_0a^3\left[M(k_2a)^2(4\alpha\mu L - 2L^2 - 3\alpha^2\mu^2) - 10H\mu(L-\mu)\right]}{15\pi H\mu(L-\mu)}. \tag{5.13}$$

Thus equation (5.2) yields

$$f_{low}(0) = \frac{\left[5 + \frac{M(2-4\alpha g+3\alpha^2g^2)(k_2a)^2}{2Hg(1-g)}\right](H-\alpha M)^2k_1^2a^3}{15\pi\mu H(1-g)}. \tag{5.14}$$

By substituting (5.14) into (2.23) and taking the real part, one can obtain an expression for effective velocity in the low frequency limit

$$v^* = v_1\left[1 - \frac{2\varepsilon(H-\alpha M)^2}{3\mu H(1-g)}\right]. \tag{5.15}$$

In (5.15) $v_1 = \omega/k_1 = (H/\rho)^{1/2}$ is the velocity of the fast compressional wave in the porous host (crack-free fluid-saturated porous medium) and $\varepsilon = n_0a^3 = (3/4\pi)(a/b)\phi_c$ is the crack density parameter (Hudson, 1980) where $\phi_c = (4/3)\pi a^2bn_0$ is the additional porosity present due to the cracks.

Low-frequency attenuation Q^{-1} is defined by the imaginary part of the function $f_{low}(0)$,

$$Q_{low}^{-1} = \frac{2M(H-\alpha M)^2(2-4\alpha g+3\alpha^2g^2)\left|k_2a\right|^2\varepsilon}{15\mu H^2g(1-g)^2}, \tag{5.16}$$

and is proportional to $|k_2a|^2$, that is, to the first power of frequency.

High frequency asymptote

For high frequencies $|k_2|\, a \gg 1$. To analyse this case we note that function $R(x, y)$ as given by (4.55) is a function oscillating with a period of $2\pi/a$ and decaying with y as y^{-1}. At the same time, T is also a function decaying with a positive power of y. Thus most of the contribution to the integral in equation (4.54) comes from the interval $0 < y < y_0$,that is,

$$B(x) + \frac{1}{\pi} \int_0^{y_0} R(x, y) T(y) B(y) dy \approx -p_0 S(x), \tag{5.17}$$

where y_0 is on the order of $1/a$. For high frequencies $|k_2|\, a \gg 1$ and thus $y_0 \ll |k_2|$. Hence I can simplify expression (5.3) assuming that $y \ll |k_2|$,

$$T_{high}(y) \approx \frac{-iML^2 k_2}{2H\mu(L-\mu)y}. \tag{5.18}$$

In this limit I can obtain an analytical solution directly from dual equations (4.42) and (4.43). Since $T_{high}(y)$ is much larger than 1 in equation (4.42), substituting $T_{high}(y)$ yields a single integral equation for $B(y)$:

$$\int_0^{\infty} B(y) J_0(yr)\, dy = D(r), \tag{5.19}$$

where

$$D(r) = \begin{array}{ll} \frac{-2igH(1-g)p_0}{Mk_2} & 0 \le r \le a \\ 0 & a < r \le \infty \end{array}. \tag{5.20}$$

Note that the left hand side of (5.19) is simply the Hankel transform of the function $B(y)/y$. Thus $B(y)/y$ can be obtained as the inverse Hankel transform of the right hand side,

$$\frac{B(y)}{y} = \int_0^{\infty} D(r) J_0(yr)\, r dr = \frac{-2igH(1-g)p_0}{Mk_2} \int_0^{a} J_0(yr)\, r dr.$$

For equation (5.2) I only need the limit of $B(y)/y$ for small y. Noting that $J_0(yr) \to 1$ for small arguments, I obtain

$$\lim_{y\to 0} \frac{B(y)}{y} = \frac{-igH(1-g)p_0a^2}{Mk_2}. \tag{5.21}$$

Substitution of this result into equation (5.2) yields:

$$f_{high}(0) = -\frac{i(k_1a)^2(H-\alpha M)^2}{2MLk_2}. \tag{5.22}$$

By substituting this expression into the dispersion equation (2.23) one can see that its relative contribution to the real part of the effective wavenumber vanishes in the high frequency limit, implying that the velocity in that limit tends to the velocity in the porous crack-free medium. This result is logical as at sufficiently high frequencies the fluid has no time to move between pores and cracks, and therefore the cracks behave as if they were isolated. In particular, the dry case is excluded, except in the static limit.

Attenuation at high frequencies reads

$$Q_{high}^{-1} = \frac{\sqrt{2}\pi\varepsilon(H-\alpha M)^2}{ML\,|k_2a|}, \tag{5.23}$$

and thus scales with $\omega^{-1/2}$.

5.4 Discussion

5.4.1 The dry limit

Generally speaking, the results of the preceding sections are based on the assumption $K_f/\mu \gg c/a$, and therefore do not apply in the dry limit $K_f \to 0$. Indeed, at finite frequencies a dry limit does not make sense because this is a dynamic situation in which the overall medium takes on an additional stiffness as a result of the fluid in the crack resisting compression of the pore space. I can take this limit in the low-fequency limit,

however. At low frequencies I have a quasi-static situation in which fluid pressure has plenty of time to equilibrate throughout all of the porosity in response to deformation of the medium, whether that be background equant pores or penny-shaped cracks. Since the fluid in the crack has adequate time to flow it doesn't significantly affect the elastic properties of the overall medium. Thus, for dry open cracks, $K_f = M = 0$, $H = K + 4\mu/3$ and equation (5.15) simplifies to

$$v^* = v_1 \left[1 - \frac{2\varepsilon}{3g(1-g)} \right], \tag{5.24}$$

which coincides with the well-known expression for the velocity of compressional waves propagating perpendicular to a system of dry open cracks in an elastic medium in the limit of low crack density (Hudson, 1980). This agreement makes sense because in the case of a dry medium, assumptions about fluid flow are irrelevant.

5.4.2 Gassmann consistency

In the low frequency limit the pressure throughout the pore space and fractures should be equlibrated. In his seminal paper Gassmann (1951) showed that in this case the elastic properties of the saturated medium are uniquely defined by the elastic properties of the dry frame, porosity, and the bulk moduli of the solid grain material and the saturating fluid. For the isotropic case Gassmann derived his famous equation for the undrained bulk modulus of the saturated medium which is widely used for fluid substitution in porous rocks. But Gassmann (1951) also derived a more general equation for the case where the frame is macroscopically anisotropic (but is still made up of a single isotropic solid material). This equation was later generalised by Brown & Korringa (1975) to materials made of anisotropic and microheterogeneous solid material.

A porous medium with aligned fractures is macroscopically anisotropic (transversely isotropic) and is made of one isotropic solid and therefore should be consistent with the anisotropic Gassmann (1951) equation. This particular case was analysed by Gurevich

(2003) who derived explicit expressions for the stiffness tensor of the saturated medium as a function of porosity and elastic moduli of the background medium, solid and fluid bulk moduli, and fracture weakness (which can be related to fracture density for sparsely populated cracks).

The results of Gurevich (2003) are exact expressions valid for any fracture weakness. In order to compare my low-frequency result with the expression of Gurevich (2003), I expand that expression in powers of fracture density and retain only the linear term. The resulting expression for the plane deformation stifffness c_{33}^{sat} along the symmetry axis z is

$$c_{33}^{sat} = H\left[1 - \frac{4\varepsilon(H-\alpha M)^2}{3\mu H(1-g)}\right]. \tag{5.25}$$

For compressional velocity along the z axis equation (5.25) is identical to (5.15) (again, for small crack density). This confirms that my result at low frequencies is asymptotically (e.g., in the sparse limit) consistent with Gassmann's theory. This Gassmann consistency is an important feature of the model presented here and shows that the hydraulic interaction between cracks is accounted for.

5.4.3 Comparison with the equant porosity model of Hudson et al. (1996)

I can compare the predictions of my model with the equant porosity model (EPM) of Hudson et al. (1996) as the two models differ only in the assumptions that have been made regarding fluid flow, all the parameters are the same. The effective velocity for wave propagation in the EPM is

$$v_H^* = v_{1H}\left[1 - \frac{4\varepsilon L^2}{3\mu(1+K_H)(L-\mu)}\right], \tag{5.26}$$

where for thin cracks

$$K_H \approx \left(\frac{1+i}{3}\right)\frac{L}{\mu}\left(\frac{K_f}{L-\mu}\right)\frac{a}{J}, \tag{5.27}$$

and

$$J^2 = \frac{\phi K_f \kappa}{2\omega\eta}. \tag{5.28}$$

Figure 5-2 shows the dispersion predicted by both models as well as high and low frequency asymptotes for my model. At high frequencies both models predict no deviation from the background velocity. This is logical as in the high frequency limit of both models there is no time available for appreciable fluid flow to occur, and hence there will be no flow-induced dispersion. At low frequencies our model is consistent with the static Gassmann theory, whereas the EPM is not. The reason for this disagreement is that hydraulic interaction between cracks is not accounted for in the EPM.

Figure 5-3 shows the attenuation curves for both models, and the low and high frequency asymptotes for my model. The attenuation asymptotes for the EPM are

$$Q^{-1}_{lowH} = \frac{8\sqrt{2}\varepsilon a}{9\mu g(1-g)^2}\sqrt{\frac{K_f\eta\omega}{\phi\kappa}}, \tag{5.29}$$

for low frequencies and

$$Q^{-1}_{highH} = \frac{2\sqrt{2}\varepsilon L}{K_f a}\sqrt{\frac{\phi K_f\kappa}{\eta\omega}}, \tag{5.30}$$

for high frequencies. I can more closely compare my asymptotes (5.16) and (5.23) with the EPM by taking a rigid-frame approximation, which yields

$$Q^{-1}_{low} \approx \frac{4(2-4\alpha g+3\alpha^2 g^2)a^2\varepsilon\eta\omega}{15\mu g(1-g)^2\kappa}, \tag{5.31}$$

for low frequencies and

$$Q^{-1}_{high} \approx \frac{\sqrt{2}\pi\varepsilon L}{3K_f a}\sqrt{\frac{\phi K_f\kappa}{\eta\omega}}, \tag{5.32}$$

for high frequencies. At high frequencies the behaviour of my model is almost identical to that of the EPM, apart from the factor of $2\pi/3$. At low frequencies the predictions are significantly different, as my model predicts that Q^{-1}will be proportional to ω whereas the EPM predicts Q^{-1} being proportional to $\sqrt{\omega}$. The attenuation curves of Figure 5-3

also show that both models predict an attenuation peak of the same magnitude, although the EPM predicts the peak occurring at a lower frequency.

An approximation for the nature of the characteristic attenuation peaks shown in Figure 5-3 can be obtained by considering the frequency at which the low and high frequency asymptotes intersect. The intersection frequency for my model is

$$\omega = \frac{\kappa K_f}{\eta a^2 \phi} \left(\frac{5\sqrt{2}\pi\mu^2\phi^2}{2K_f^2} \right)^{2/3}, \tag{5.33}$$

and for the EPM is

$$\omega = \frac{9\kappa\phi\mu^2(1-g)^2}{4\eta a^2 K_f}. \tag{5.34}$$

These expressions have similar dependencies on permeability, fluid viscosity and crack radius, but differ with regards to fluid modulus and porosity.

5.4.4 Comparison with spherical inclusions

The analogous scattering problem for the case of a sparse distribution of spherical inclusions in a porous medium was treated by Ciz et al. (2006). The attenuation curve for the case of identical material parameters and fluid filled cavities is also shown in Figure 5-3. Note that the dependence on frequency is identical for the high and low frequency asymptotic behaviour, only the magnitude is different. This is due to the fact that a thin crack is more compliant to deformation than a sphere, and therefore there is always going to be more fluid flow induced attenuation taking place in the medium with cracks. At low frequencies the curves are quite close, implying that at these wavelengths the small scale differences between a sphere and a crack of the same radius do not have a great effect on the attenuation, they are both behaving like point scatterers. At higher frequencies however there is a larger difference between spherical and crack-like inclusions as wavelengths are small enough for the small scale differences to be noticed.

Chapter 6

Conclusions and Recommendations

In this thesis I have investigated the effect that aligned fracturing has on the elastic wave attenuation, dispersion and anisotropy in fluid-saturated porous media. I have quantified the long-wavelength effective anisotropy that results from aligned fractures in the presence of equant porosity and the attenuation and dispersion due to wave-induced fluid flow between the compliant fractures and the pores in the stiffer host medium.

6.1 Fluid-dependent Shear-wave Splitting in a Fractured Poroelastic Medium

One of the issues I addressed is the effect of fracture-filling fluid properties on the shear-wave splitting taking place in a fractured porous medium. If shear deformation is in any way coupled with compressional deformation, the shear-wave splitting will depend upon the compressibility of the saturating fluid. In this case, the coupling is a result of the effective anisotropy brought about by the presence of aligned fracturing. If the fractures and pores are hydraulically connected, the contribution of the fluid compressibility to the overall elastic properties of the medium will depend upon the extent to which fluid pressure can equilibrate during deformation. Hence I conclude that the dependency of the shear-wave splitting on the fluid bulk modulus will be at its minimum for quasi-

static deformations, and will increase with increasing wave frequency. Further studies are needed to quantify this frequency dependency explicitly and to determine to what extent the analysis of shear-wave splitting can determine the fracture-filling fluid type..

6.2 Scattering by a Single Crack in a Poroelastic Medium

In order to model fracturing using discrete flat circular cracks, I solved the scattering problem for such a crack embedded in a fluid-saturated porous host. The fundamental difference between poroelasticity and elasticity is the phenomenon of fluid flow occurring relative to the solid skeleton. The scattering that occurs in this medium is predominantly because of fluid diffusion in and out of the crack, hence the scattering cross section takes it's maximum value around the dimensionless frequency $|k_2 a|^2 = 1$, where the conversion of incident energy into the slow wave is at it's most efficient. For frequencies such that the crack is small compared to the wavelength, w_z is distributed uniformly amongst the radial wavenumbers so that the crack behaves like a point scatterer with no preferred directionality. As frequencies increase, however, the dominant radial wavenumbers are those closer to zero, as when the wavelength is comparable to the crack radius w_z tends to occur perpendicular to the crack surface, as would be expected. I conclude that this poroelastic effect should not be neglected, at least at seismic frequencies.

6.3 Effective Properties of a Poroelastic Medium Containing a Distribution of Aligned Cracks

When the effect of a distribution of cracks is considered, assumptions regarding the interaction between individual cracks govern how realistic the model is. I estimate the effect of a distribution of cracks using the multiple-scattering theorem of Waterman

& Truell (1961). This theory accounts for the interaction between scatterers (i.e the multiple scattering) as long as the cracks are not too close together (small crack density). I obtain from this analysis an effective velocity which at low frequencies reduces to the known static Gassmann result. When the interaction between cracks is neglected, such as in the EPM of Hudson et al. (1996), a result is obtained that does not reduce to the static Gassmann limit. Hence I conclude that the interaction between cracks should not be neglected even in the limit of weak crack density. The disagreement between the attenuation predicted by both models at low frequencies is also a manifestation of the fundamental difference between the two models regarding the interaction between cracks. Since the models only agree with each other at high frequencies, when the time available for fluid diffusion is small, I conclude that the interaction between cracks that takes place as a result of fluid diffusion is negligible at high frequencies.

The comparison between the model presented here and the model for spherical inclusions sheds some light on the effect of inclusion shape on the effective properties of the medium. As seen on the attenuation plot (Figure 5-3) the attenuation for spherical inclusions has exactly the same dependence upon frequency, but a difference in magnitude that depends upon frequency. Since the attenuation curves are very close at low frequencies I conclude that the effective medium properties are not sensitive to the shape of an inclusion at wavelengths that are large compared to the inclusion size. However at frequencies such that the wavelength is comparable to or smaller than the inclusion size the effective properties are sensitive to the greater compliance of the flat cracks, and more attenuation occurs at a given frequency as a result.

The scattering analysis performed in this thesis was limited to the preliminary case of normal incidence. It is recommended that the more general problem of scattering of a wave at oblique incidence be treated, as this would allow the determination of the effective anisotropy of the medium due to the cracks. This problem has been treated for elastic media by Garbin & Knopoff (1973). In a preliminary investigation performed at the end of my research I found that the general solution to Biot's equations can be found

for the case of oblique incidence by using the more general Fourier-Bessel series solution (see, for example, the Basic Formulation section of Shams-Zadeh-Amiri et al. (2003), who treat an analogous electromagnetic radiation problem). The boundary conditions for the case of oblique incidence will also be more complicated.

A limitation of the analysis performed in this thesis is that it is only valid for the case of weak crack densities. A recommended topic for future research is to extend this type of analysis to allow for higher crack densities, see for example Zhang & Achenbach (1991).

Bibliography

Auriault, J.-L. & Boutin, C. (1994). Deformable porous media with double porosity III: Acoustics. *Transport in Porous Media*, 14, 143–162.

Bakulin, A., Grechka, V., & Tsvankin, I. (2000a). Estimation of fracture parameters from reflection seismic data – Part I: HTI model due to a single fracture set. *Geophysics*, 65, 1788–1802.

Bakulin, A., Grechka, V., & Tsvankin, I. (2000b). Estimation of fracture parameters from reflection seismic data – Part III: Fractured models with monoclinic symmetry. *Geophysics*, 65, 1818–1830.

Biot, M. A. (1956). Theory of propagation of elastic waves in a fluid-saturated porous solid. I. Low-frequency range. *J. Acoust. Soc. Amer.*, 28, 168–178.

Biot, M. A. (1962). Mechanics of deformation and acoustic propagation in porous media. *J. Appl. Phys.*, 33, 1482–1498.

Biot, M. A. & Willis, D. G. (1957). The elastic co-efficients of the theory of consolidation. *J. App. Mech.*, 24, 594–601.

Brajanovski, M., Gurevich, B., & Schoenberg, M. (2005). A model for P-wave attenuation and dispersion in a porous medium permeated by aligned fractures. *Geophys. J. Internat.*, 163, 372–384.

Brown, L. & Gurevich, B. (2004). Frequency-dependent seismic anisotropy of porous rocks with penny-shaped cracks. *Exploration Geophysics*, 35(2), 111–115.

Brown, R. J. S. & Korringa, J. (1975). On the dependence of the elastic properties of a porous rock on the compressibility of the pore fluid. *Geophysics*, 40, 608–616.

Cardona, R. (2002). Two theories for fluid substitution in porous rocks with aligned cracks. In *72st Ann. Internat. Mtg., Soc. Expl. Geophys., Expanded Abstracts* (pp. 173–176).

Cardona, R., Batzle, M., & Davis, T. (2001). Shear wave velocity dependence on fluid saturation. In *71st Ann. Internat. Mtg., Soc. Expl. Geophys., Expanded Abstracts* (pp. 1712–1715).

Chapman, M. (2003). Frequency dependent anisotropy due to meso-scale fractures in the presence of equant porosity. *Geophys. Prosp.*, 51, 369–379.

Ciz, R., Gurevich, B., & Markov, M. (2006). Seismic attenuation due to wave-induced fluid flow in a porous rock with spherical heterogeneities. *Geophys. J. Internat.*, 165, 957–968.

Crampin, S. (1985). Evaluation of anisotropy by shear-wave splitting. *Geophysics*, 50, 142–152.

Deresiewicz, H. & Skalak, R. (1963). On uniqueness in dynamic poroelasicity. *Bull. Seismol. Soc. Amer.*, 53, 783–788.

Galvin, R. J. & Gurevich, B. (2006). Interaction of an elastic wave with a circular crack in a fluid-saturated porous medium. *Appl. Phys. Lett.*, 88, 061918.

Garbin, H. D. & Knopoff, L. (1973). The compressional modulus of a material permeated by a random distribution of circular cracks. *Quart. App. Math.*, 30, 453–464.

Gassmann, F. (1951). Über die elastizität poröser medien. *Viertel. Naturforsch. Ges. Zürich*, 96, 1–23.

Grechka, V. & Kachanov, M. (2006). Effective elasticity of fractured rocks. *The Leading Edge*, 25, 152–155.

Guest, S., van der Kolk, C., & Potters, H. (1998). The effect of fracture filling liquids on shear-wave propagation. In *68th Ann. Internat. Mtg., Soc. Expl. Geophys., Expanded Abstracts*.

Gurevich, B. (2003). Elastic properties of saturated porous rocks with aligned fractures. *Journal of Applied Geophysics*, 54, 203–218.

Helbig, K. (1994). *Foundations of Anisotropy for Exploration Seismics*. Pergamon.

Hoenig, A. (1979). Elastic moduli of a non-randomly cracked body. *International Journal of Solids and Structures*, 15, 137–154.

Hsu, C.-J. & Schoenberg, M. (1993). Elastic waves through a simulated fractured medium. *Geophysics*, 58, 964–977.

Hudson, J., Pointer, T., & Liu, E. (2001). Effective-medium theories for fluid-saturated materials with aligned cracks. *Geophys. Prosp.*, 49, 509–522.

Hudson, J. A. (1980). Overall properties of a cracked solid. *Math. Proc. Camb. Phil. Soc.*, 88, 371–384.

Hudson, J. A. (1981). Wave speeds and attenuation of elastic waves in material containing cracks. *Geophys. J. Roy. Astr. Soc.*, 64, 133–150.

Hudson, J. A. & Crampin, S. (2003). Comment on: 'The 3D shear experiment over the Natih field in Oman: the effects of fracture-filling fluids on shear propagation' by C.M. van der Kolk, W.S. Guest and J.H.H.M. Potters. *Geophysical Prospecting*, 51, 365–368.

Hudson, J. A., Liu, E., & Crampin, S. (1996). The mechanical properties of materials with interconnected cracks and pores. *Geophys. J. Internat.*, 124, 105–112.

Jakobsen, M., Johansen, T. A., & McCann, C. (2003). The acoustic signature of fluid flow in complex porous media. *Journal of Applied Geophysics*, 54, 219–246.

Jin, B. & Zhong, Z. (2002). Dynamic stress intensity factor (mode I) of a penny-shaped crack in an infinite poroelastic solid. *Int. J. Eng. Sci.*, 40, 637–646.

Maultzsch, S., Chapman, M., Liu, E., & Li, X. (2003). Modelling frequency-dependent seismic anisotropy in fluid-saturated rock with aligned fractures: implication of fracture size estimation from anisotropic measurements. *Geophysical Prospecting*, 51, 381–392.

Mavko, G., Mukerji, T., & Dvorkin, J. (1998). *The Rock Physics Handbook: Tools for Seismic Analysis in Porous Media*. Cambridge University Press.

Nakagawa, S., Nihei, K. T., & Myer, L. R. (2000). Shear-induced conversion of seismic waves across single fractures. *International Journal of Rock Mechanics and Mining Sciences*, 37, 203–218.

Nelson, R. A. (2001). *Geologic Analysis of Naturally Fractured Reservoirs*. Boston: Gulf Professional Publishing.

Noble, B. (1963). The solution of Bessel function dual integral equations by a multiplying-factor method. *Proc. Camb. Phil. Soc.*, 59, 351–362.

Nye, J. F. (1985). *Physical Properties of Crystals*. Oxford University Press.

O'Connell, R. J. & Budiansky, B. (1974). Seismic velocities in dry and saturated cracked solids. *J. Geophys. Res.*, 79, 5412–5426.

Piau, M. (1979). Attenuation of a plane compressional wave by a random distribution of thin circular cracks. *Int. J. Eng. Sci.*, 17, 151–167.

Pointer, T., Liu, E., & Hudson, J. A. (2000). Seismic wave propagation in cracked porous media. *Geophys. J. Internat.*, 142, 199–231.

Pride, S. R. & Berryman, J. G. (2003). Linear dynamics of double-porosity dual-permeability materials, 1. governing equations and acoustic attenuation. *Physical Review E.*

Reiss, L. H. (1980). *The Reservoir Engineering Aspects of Fractured Formations*. Paris: Editions Technip.

Rice, J. R. & Cleary, M. P. (1976). Some basic stress diffusion solutions for fluid-saturated elastic porous media with compressible constituents. *Reviews of Geophysics and Space Physics*, 14, 227–241.

Robertson, I. A. (1967). Diffraction of a plane longitudinal wave by a penny-shaped crack. *Proc. Camb. Phil. Soc.*, 63, 229–238.

Sayers, C. M. (2002). Fluid-dependent shear-wave splitting in fractured media. *Geophysical Prospecting*, 50, 393–401.

Sayers, C. M. & Kachanov, M. (1995). Microcrack-induced elastic wave anisotropy of brittle rocks. *Journal of Geophysical Research*, B 100, 4149–4156.

Schoenberg, M. (1980). Elastic wave behavior across linear slip interfaces. *J. Acoust. Soc. Amer.*, 68, 1516–1521.

Schoenberg, M. & Douma, J. (1988). Elastic-wave propagation in media with parallel fractures and aligned cracks. *Geophys. Prosp.*, 36, 571–590.

Schoenberg, M. & Sayers, C. M. (1995). Seismic anisotropy of fractured rock. *Geophysics*, 60, 204–211.

Shams-Zadeh-Amiri, A. M., Li, X., & Huang, W. (2003). Hankel transform-domain analysis of scattered fields in multilayer planar waveguides and lasers with circular gratings. *IEEE Journal of Quantum Electronics*, 39, 1086–1098.

Sherief, H. H. & El-Maghraby, N. M. (2003). An internal penny-shaped crack in an infinite thermoelastic solid. *J. Therm. Stresses*, 26, 333–352.

Thomsen, L. (1986). Weak elastic anisotropy. *Geophysics*, 51, 1954–1966.

Thomsen, L. (1995). Elastic anisotropy due to aligned cracks in porous rock. *Geophysical Prospecting*, 43, 805–829.

Tod, S. R. (2001). The effects on seismic waves of interconnected nearly aligned cracks. *Geophys. J. Internat.*, 146, 249–263.

van der Kolk, C., Guest, W. S., & Potters, J. H. H. M. (2001). The 3D shear experiment over the Natih field in Oman: the effect of fracture-filling fluids on shear propagation. *Geophysical Prospecting*, 49, 179–197.

Waterman, P. C. & Truell, R. (1961). Multiple scattering of waves. *J. Math. Phys.*, 2, 512–537.

Zhang, C. & Achenbach, J. D. (1991). Effective wave velocity and attenuation in a material with distributed penny-shaped cracks. *International Journal of Solids and Structures*, 27, 751–767.

Every reasonable effort has been made to acknowledge the owners of copyright material. I would be pleased to hear from any copyright owner who has been omitted or incorrectly acknowledged.

Appendix A

Chapter 3 MATLAB Code

This appendix contains the MATLAB code used to produce the results of Chapter 3. "singlefracture.m" calculates the shear-wave velocities and splitting for the case of a single fracture set. "pressureequilibrium.m" calculates the shear-wave velocities and splitting for the case of conjugate fracture sets in full pressure communication. "noninteracting.m" calculates the shear-wave velocities and splitting for the case of non-interacting fracture sets.

A.1 singlefracture.m

```
clear all;
figure;
grid on;

hold;
count=1;
for i=0:0.0025*10^9:2.5*10^9
    Kf(count)=i+0.00001;
```

```
    count=count+1;
end

for THETA=0:pi/12:pi/2
for i=1:length(Kf)

Vp_dry=4000;
Vs_fast_dry=1700;
Vs_slow_dry=1445;
phi_b=0.1;

% calcite

rho_m=2870;
rho_dry=rho_m*(1-phi_b);
mu_dry=Vs_fast_dry^2*rho_dry;
Kdry=Vp_dry^2*rho_dry-4*mu_dry/3;
Km=70*10^9;
alpha0=1-Kdry/Km;
gamma0=((Vs_fast_dry-Vs_slow_dry)/Vs_fast_dry);
deltaT=2*gamma0/(2*gamma0+1);
Zt=deltaT/(mu_dry-deltaT*mu_dry);

% assume Zn=Zt

Zn=Zt;
lambda_dry=Kdry-2*mu_dry/3;
lambda=lambda_dry;
```

```
deltaN=(lambda_dry+2*mu_dry)*Zn/(1+(lambda_dry+2*mu_dry)*Zn);
L=lambda_dry+2*mu_dry;
epsilon0=2*mu_dry*(lambda_dry+mu_dry)*deltaN/(L^2*(1-deltaN));
phi_c=0;
rho_f=1000;
rho_sat=rho_dry+(phi_b+phi_c)*rho_f;
phi=phi_b+phi_c;
M=1/((alpha0-phi)/Km+phi/Kf(i));
Ksat=Kdry+alpha0^2*M;
Lsat=Ksat+4*mu_dry/3;
lambda_sat=Lsat-2*mu_dry;
D=1+(Kf(i)/(Km*phi))*(alpha0-phi+(Kdry^2*deltaN)/(Km*L));
theta=1-(Kf(i)/Km);
alpha_prime=alpha0+(Kdry^2/(Km*L))*deltaN;
L1=Km+4*mu_dry/3;
lambda1=Km-2*mu_dry/3;
d1=1-deltaN;
d2=1-lambda_dry^2*deltaN/L^2;
c11sat=(L/D)*(d1*theta+(Kf(i)/(phi*Km*L))*(L1*alpha_prime-...
(16*mu_dry^2*alpha0*deltaN)/(9*L)));
c33sat=(L/D)*(d2*theta+(Kf(i)/(phi*Km*L))*(L1*alpha_prime-...
(4*mu_dry^2*alpha0*deltaN)/(9*L)));
c13sat=(lambda/D)*(d1*theta+(Kf(i)/(phi*Km*lambda))*...
(lambda1*alpha_prime+(8*mu_dry^2*alpha0*deltaN)/(9*L)));
c13sat-lambda*(1-deltaN)
c44sat=mu_dry;
c55sat=mu_dry*(1-deltaT);
m=sqrt(((c33sat-c55sat)*sin(THETA)^2-(c11sat-c55sat)*cos(THETA)^2)...
```

```
^2+(c13sat+c55sat)^2*sin(2*THETA)^2);
Vp_sat(i)=sqrt(c33sat*sin(THETA)^2+c11sat*cos(THETA)^2+c55sat+m)...
/sqrt(2*rho_sat);
Vs2_sat=sqrt(c33sat*sin(THETA)^2+c11sat*cos(THETA)^2+c55sat-m)...
/sqrt(2*rho_sat);
VS2(i)=Vs2_sat;
Vs1_sat=sqrt((c44sat*sin(THETA)^2+c55sat*cos(THETA)^2)/rho_sat);
VS1(i)=Vs1_sat;
epsilon_sat=(c33sat-c11sat)/(2*c11sat);
gamma_sat=(c44sat-c55sat)/(2*c55sat);
delta_sat=((c13sat+c55sat)^2-(c11sat-c55sat)^2)/(2*c11sat*...
(c11sat-c55sat));
Zn_sat=Zn*Lsat*(lambda+mu_dry)*epsilon_sat/(L*(lambda_sat+mu_dry)...
*epsilon0);
splitting(i)=(Vs1_sat^2-Vs2_sat^2)/(Vs1_sat^2+Vs2_sat^2);

end

     plot(Kf,VS1,'--',Kf,VS2);
      plot(Kf,splitting);
%     axis([0 2.5*10^9 -0.05 0.25]);
%     axis normal;

   xlabel('K_f')
     ylabel('s')
% ylabel('Vp');
end
```

A.2 pressureequilibrium.m

```
clear all;
figure;
hold;
count=1;

for i=0:0.025*10^9:2.5*10^9
    Kf(count)=i+0.00001;
    count=count+1;
end

for theta=0:pi/12:pi/2

    for i=1:length(Kf)

Vp_dry=4000;
Vs_fast_dry=1700;
Vs_slow_dry=1445;
phi_b=0.1;

% calcite

rho_m=2870;
rho_dry=rho_m*(1-phi_b);
mu_dry=Vs_fast_dry^2*rho_dry;
mu=mu_dry;
Kdry=Vp_dry^2*rho_dry-4*mu_dry/3;
Km=70*10^9;
```

```
alpha0=1-Kdry/Km;
gamma0=((Vs_fast_dry-Vs_slow_dry)/Vs_fast_dry);
deltaT=2*gamma0/(2*gamma0+1);
Zt=deltaT/(mu_dry-deltaT*mu_dry);

% assume Zn=Zt

Zn=Zt;
lambda_dry=Kdry-2*mu_dry/3;
lambda=lambda_dry;
deltaN=(lambda_dry+2*mu_dry)*Zn/(1+(lambda_dry+2*mu_dry)*Zn);
L=lambda_dry+2*mu_dry;
%epsilon0=2*mu_dry*(lambda_dry+mu_dry)*deltaN/(L^2*(1-deltaN));
phi_c=0;
rho_f=1000;
rho_sat=rho_dry+(phi_b+phi_c)*rho_f;
phi=(phi_b+phi_c);
Zt1=Zt;
Zt2=0.5*Zt1;
alpha11=(Zt1+Zt2)*cos(theta)^2;
alpha13=(Zt2-Zt1)*cos(theta)*sin(theta);
alpha33=(Zt1+Zt2)*sin(theta)^2;
S011=(lambda+mu)/(mu*(3*lambda+2*mu));
S012=-1*lambda/(2*mu*(3*lambda+2*mu));
S013=S012;
S021=S012;
S022=S011;
S023=S012;
```

```
S031=S012;
S032=S012;
S033=S011;
S044=1/mu;
S055=S044;
S066=S044;

S0=[S011 S012 S013 0 0 0
    S021 S022 S023 0 0 0
    S031 S032 S033 0 0 0
    0 0 0 S044 0 0
    0 0 0 0 S055 0
    0 0 0 0 0 S066];

deltaS11=alpha11;
deltaS33=alpha33;
deltaS44=alpha33;
deltaS46=alpha13;
deltaS55=alpha33+alpha11;
deltaS66=alpha11;
deltaS15=alpha13;
deltaS35=alpha13;

deltaS=[deltaS11 0 0 0 deltaS15 0
    0 0 0 0 0 0
    0 0 deltaS33 0 deltaS35 0
    0 0 0 deltaS44 0 deltaS46
    deltaS15 0 deltaS35 0 deltaS55 0
```

```
    0 0 0 deltaS46 0 deltaS66];

S=S0+deltaS;
C=inv(S);

% Effect of saturating fluid

alpha=1/(phi*(1/Kf(i)-1/Km));
b1=1-(C(1,1)+C(1,2)+C(1,3))/(3*Km);
b2=1-(C(2,1)+C(2,2)+C(2,3))/(3*Km);
b3=1-(C(3,1)+C(3,2)+C(3,3))/(3*Km);
b4=-1*(C(4,1)+C(4,2)+C(4,3))/(3*Km);
b5=-1*(C(5,1)+C(5,2)+C(5,3))/(3*Km);
b6=-1*(C(6,1)+C(6,2)+C(6,3))/(3*Km);
Dstar=1+(alpha/(3*Km))*(b1+b2+b3);
c11sat=C(1,1)+b1^2*alpha/Dstar;
c22sat=C(2,2)+b2^2*alpha/Dstar;
c33sat=C(3,3)+b3^2*alpha/Dstar;
c44sat=C(4,4)+b4^2*alpha/Dstar;
c55sat=C(5,5)+b5^2*alpha/Dstar;
c66sat=C(6,6)+b6^2*alpha/Dstar;
c12sat=C(1,2)+b1*b2*alpha/Dstar;
c13sat=C(1,3)+b1*b3*alpha/Dstar;
c14sat=C(1,4)+b1*b4*alpha/Dstar;
c15sat=C(1,5)+b1*b5*alpha/Dstar;
c16sat=C(1,6)+b1*b6*alpha/Dstar;
c23sat=C(2,3)+b2*b3*alpha/Dstar;
c24sat=C(2,4)+b2*b4*alpha/Dstar;
```

```
c25sat=C(2,5)+b2*b5*alpha/Dstar;
c26sat=C(2,6)+b2*b6*alpha/Dstar;
c34sat=C(3,4)+b3*b4*alpha/Dstar;
c35sat=C(3,5)+b3*b5*alpha/Dstar;
c36sat=C(3,6)+b3*b6*alpha/Dstar;
c45sat=C(4,5)+b4*b5*alpha/Dstar;
c46sat=C(4,6)+b4*b6*alpha/Dstar;
c56sat=C(5,6)+b5*b6*alpha/Dstar;

Vs2=sqrt((2/rho_sat)*(c33sat*c55sat-c35sat^2)/(c33sat+c55sat+...
sqrt((c33sat-c55sat)^2+4*c35sat^2)));
VS2(i)=Vs2;
Vs1=sqrt(c44sat/rho_sat);
VS1(i)=Vs1;
splitting(i)=(Vs1^2-Vs2^2)/(Vs1^2+Vs2^2);

    end

%      plot(Kf,VS2);
%    plot(Kf,Vs2_sat);
     plot(Kf,splitting);
    xlabel('K_f')
    ylabel('s')
%    ylabel('Vs')
end
```

A.3 noninteracting.m

```
clear all;
format short
figure;
hold;
count=1;

for i=0:0.025*10^9:2.5*10^9
    Kf(count)=i+0.00001;
    count=count+1;
end

for THETA=0:pi/12:pi/2;
    for i=1:length(Kf)

Vp_dry=4000;
Vs_fast_dry=1700;
Vs_slow_dry=1445;
phi_b=0.1;

% calcite

rho_m=2870;
rho_dry=rho_m*(1-phi_b);
mu_dry=Vs_fast_dry^2*rho_dry;
mu=mu_dry;
Kdry=Vp_dry^2*rho_dry-4*mu_dry/3;
Km=70*10^9;
```

```
alpha0=1-Kdry/Km;
gamma0=((Vs_fast_dry-Vs_slow_dry)/Vs_fast_dry);
deltaT=2*gamma0/(2*gamma0+1);
Zt=deltaT/(mu_dry-deltaT*mu_dry);

% assume Zn=Zt

Zn=Zt;
lambda_dry=Kdry-2*mu_dry/3;
lambda=lambda_dry;
phi_c=0;
phi=(phi_b+phi_c);

C0=[lambda+2*mu lambda lambda 0 0 0
    lambda lambda+2*mu lambda 0 0 0
    lambda lambda lambda+2*mu 0 0 0
    0 0 0 mu 0 0
    0 0 0 0 mu 0
    0 0 0 0 0 mu];

% Effect of saturating fluid

alpha=1/(phi*(1/Kf(i)-1/Km));
b1=1-(C0(1,1)+C0(1,2)+C0(1,3))/(3*Km);
b2=1-(C0(2,1)+C0(2,2)+C0(2,3))/(3*Km);
b3=1-(C0(3,1)+C0(3,2)+C0(3,3))/(3*Km);
b4=-1*(C0(4,1)+C0(4,2)+C0(4,3))/(3*Km);
b5=-1*(C0(5,1)+C0(5,2)+C0(5,3))/(3*Km);
```

```
b6=-1*(C0(6,1)+C0(6,2)+C0(6,3))/(3*Km);
Dstar=1+(alpha/(3*Km))*(b1+b2+b3);
c11satB=C0(1,1)+b1^2*alpha/Dstar;
c22satB=C0(2,2)+b2^2*alpha/Dstar;
c33satB=C0(3,3)+b3^2*alpha/Dstar;
c44satB=C0(4,4)+b4^2*alpha/Dstar;
c55satB=C0(5,5)+b5^2*alpha/Dstar;
c66satB=C0(6,6)+b6^2*alpha/Dstar;
c12satB=C0(1,2)+b1*b2*alpha/Dstar;
c13satB=C0(1,3)+b1*b3*alpha/Dstar;
c14satB=C0(1,4)+b1*b4*alpha/Dstar;
c15satB=C0(1,5)+b1*b5*alpha/Dstar;
c16satB=C0(1,6)+b1*b6*alpha/Dstar;
c23satB=C0(2,3)+b2*b3*alpha/Dstar;
c24satB=C0(2,4)+b2*b4*alpha/Dstar;
c25satB=C0(2,5)+b2*b5*alpha/Dstar;
c26satB=C0(2,6)+b2*b6*alpha/Dstar;
c34satB=C0(3,4)+b3*b4*alpha/Dstar;
c35satB=C0(3,5)+b3*b5*alpha/Dstar;
c36satB=C0(3,6)+b3*b6*alpha/Dstar;
c45satB=C0(4,5)+b4*b5*alpha/Dstar;
c46satB=C0(4,6)+b4*b6*alpha/Dstar;
c56satB=C0(5,6)+b5*b6*alpha/Dstar;

Cb=[c11satB c12satB c13satB c14satB c15satB c16satB
    c12satB c22satB c23satB c24satB c25satB c26satB
    c13satB c23satB c33satB c34satB c35satB c36satB
    c14satB c24satB c34satB c44satB c45satB c46satB
```

```
    c15satB c25satB c35satB c45satB c55satB c56satB
    c16satB c26satB c36satB c46satB c56satB c66satB];

deltaN=(lambda_dry+2*mu_dry)*Zn/(1+(lambda_dry+2*mu_dry)*Zn);
L=lambda_dry+2*mu_dry;
epsilon0=2*mu_dry*(lambda_dry+mu_dry)*deltaN/(L^2*(1-deltaN));
phi_c=0;
rho_f=1000;
rho_sat=rho_dry+(phi_b+phi_c)*rho_f;
phi=(phi_b+phi_c);
M=1/((alpha0-phi)/Km+phi/Kf(i));
Ksat=Kdry+alpha0^2*M;
Lsat=Ksat+4*mu_dry/3;
lambda_sat=Lsat-2*mu_dry;
D=1+(Kf(i)/(Km*phi))*(alpha0-phi+(Kdry^2*deltaN)/(Km*L));
theta=1-(Kf(i)/Km);
alpha_prime=alpha0+(Kdry^2/(Km*L))*deltaN;
L1=Km+4*mu_dry/3;
lambda1=Km-2*mu_dry/3;
d1=1-deltaN;
d2=1-lambda_dry^2*deltaN/L^2;
c11sat=(L/D)*(d1*theta+(Kf(i)/(phi*Km*L))*(L1*alpha_prime-...
(16*mu_dry^2*alpha0*deltaN)/(9*L)));
c33sat=(L/D)*(d2*theta+(Kf(i)/(phi*Km*L))*(L1*alpha_prime-...
(4*mu_dry^2*alpha0*deltaN)/(9*L)));
c13sat=(lambda/D)*(d1*theta+(Kf(i)/(phi*Km*lambda))*(lambda1...
*alpha_prime+(8*mu_dry^2*alpha0*deltaN)/(9*L)));
c13sat-lambda*(1-deltaN);
```

```
c44sat=mu_dry;
c55sat=mu_dry*(1-deltaT);
epsilon_sat=(c33sat-c11sat)/(2*c11sat);
gamma_sat=(c44sat-c55sat)/(2*c55sat);
delta_sat=((c13sat+c55sat)^2-(c11sat-c55sat)^2)/(2*c11sat*...
(c11sat-c55sat));
Zn_sat=Zn*Lsat*(lambda+mu_dry)*epsilon_sat/(L*(lambda_sat+...
mu_dry)*epsilon0);
Zt1=Zt;
Zt2=0.5*Zt1;
ZnSat1=Zn_sat;
ZnSat2=0.5*ZnSat1;
alpha11=(Zt1+Zt2)*cos(THETA)^2;
alpha13=(Zt2-Zt1)*cos(THETA)*sin(THETA);
alpha33=(Zt1+Zt2)*sin(THETA)^2;
B1=ZnSat1-Zt1;
B2=ZnSat2-Zt2;
beta1111=(B1+B2)*cos(THETA)^4;
beta1113=(B2-B1)*cos(THETA)^3*sin(THETA);
beta1133=(B1+B2)*cos(THETA)^2*sin(THETA)^2;
beta1313=beta1133;
beta1333=(B2-B1)*cos(THETA)*sin(THETA)^3;
beta3333=(B1+B2)*sin(THETA)^4;
S0=inv(Cb);
deltaS11=alpha11+beta1111;
deltaS33=alpha33+beta3333;
deltaS44=alpha33;
deltaS13=beta1133;
```

```
deltaS46=alpha13;
deltaS55=alpha33+alpha11+4*beta1313;
deltaS66=alpha11;
deltaS15=alpha13;
deltaS35=alpha13;

deltaS=[deltaS11 0 deltaS13 0 deltaS15 0
    0 0 0 0 0 0
    deltaS13 0 deltaS33 0 deltaS35 0
    0 0 0 deltaS44 0 deltaS46
    deltaS15 0 deltaS35 0 deltaS55 0
    0 0 0 deltaS46 0 deltaS66];

S=S0+deltaS;
C=inv(S);

Vs2=sqrt((2/rho_sat)*(C(3,3)*C(5,5)-C(3,5)^2)/(C(3,3)+C(5,5)+...
sqrt((C(3,3)-C(5,5))^2+4*C(3,5)^2)));
VS2(i)=Vs2;
Vs1=sqrt(C(4,4)/rho_sat);
VS1(i)=Vs1;
splitting(i)=(Vs1^2-Vs2^2)/(Vs1^2+Vs2^2);

    end

%      plot(Kf,VS2);
%    plot(Kf,Vs2_sat);
     plot(Kf,splitting);
```

```
    xlabel('K_f')
    ylabel('s')
%    ylabel('Vs')
end
```

Appendix B

Chapter 4 MATLAB Code

This appendix contains the MATLAB code used to produce the results of Chapter 4. "singlescattering.m" numerically solves the Fredholm integral equation obtained in Chapter 4 which allows computation of the scattered field. "lambdaK_generalf.m" is a function file referred to by "singlescattering.m". It is effectively the kernal of the Fredholm equation. "gf.m" is a function file referred to by "singlescattering.m". It is the RHS of the Fredholm equation.

B.1 singlescattering.m

```
clear all;


global kk_e h tau L_e Ldim_e mu_e k0 k1 k2 k3 kk k2_g visc perm b bdim I;
global rrr oo Kg mug Kf porosity alpha Kdry mudry taudry L Kstar M HBiot;
global Mdim HBiotdim Ldim rhodrydim A1_g A2_g q1 q2;
I=sqrt(-1);
n0=0.01;
a=1;
Kg=37*10^9;
```

```
mug=44*10^9;
Kf=2.25*10^9;
porosity=0.3;
visc=1e-3;
perm=1e-12;
rhof=1e3;
rhos=2.65e3;
rhodry=(1-porosity)*rhos;
rho=(1-porosity)*rhos+porosity*rhof;
b=visc/perm;
alpha=1-(1-porosity)^(3/(1-porosity));
Kdry=Kg*(1-alpha);
mudry=mug*(1-alpha);
bdim=b/sqrt(rho*mudry);
L=Kdry+4*mudry/3;
taudry=sqrt(mudry/L);
M=Kg/((1-Kdry/Kg)-porosity*(1-Kg/Kf));
HBiot=L+alpha^2*M;
Mdim=M/mudry;
HBiotdim=HBiot/mudry;
Ldim=L/mudry;
rhodrydim=rhodry/rho;
omegadim=[0.0001 10^-3.5 0.001 10^-2.5 0.01 10^-1.5 0.1 10^-0.5 1 ...
    10^0.5 10 10^1.5 100 10^2.5 1000 10^3.5 10000];

for q=1:length(omegadim)

    oo=omegadim(q);
```

```
    c0=sqrt(Ldim/rhodrydim);

k0=oo/sqrt(Ldim);
c1=sqrt(HBiotdim);
k1=oo/c1;
k2=sqrt(I*oo*bdim*HBiotdim/(Ldim*Mdim));
k3=oo;
kk=abs(k2);
omeg(q)=kk^2;
h=k1;
x1=0;

if kk <= 1
   spac=2*kk;
  x2=4;
   x2=200*spac;
   spac=0.1*kk;
else
   spac=0.002*kk;
   x2=40;
end

x2=max(4,kk*10);
p=-1*(HBiotdim-alpha*Mdim);

NMAX=200;
omk=eye(NMAX);
```

```
% CALCULATE GAUSS-LEGENDRE WEIGHTS

m=(NMAX+1)/2;
xm=(x2+x1)/2;
xl=(x2-x1)/2;

for i=1:m
    Z=cos(pi*(i-1/4)/(NMAX+1/2));
    Z1=Z-1;
    while (Z-Z1) > 3d-14
    p1=1;
    p2=0;
    for j=1:NMAX
        p3=p2;
        p2=p1;
        p1=((2*j-1)*Z*p2-(j-1)*p3)/j;
    end

    pp=NMAX*(Z*p1-p2)/(Z^2-1);
    Z1=Z;
    Z=Z1-p1/pp;

    end
        x(i)=xm-xl*Z;
        x(NMAX+1-i)=xm+xl*Z;
        w(i)=2*xl/((1-Z^2)*pp^2);
        w(NMAX+1-i)=w(i);
end
```

```
for i=1:NMAX

    u(i)=x(i);

end

    for j=1:NMAX
        z(j)=x(j);
    end

    for i=1:NMAX
        for j=1:NMAX
            omkk_g(i,j)=omk(i,j)-lambdaK_generalf(u(i),z(j))*w(i);
        end
    end

for j=1:NMAX
    gmat(j)=gf(z(j));
end



f_g=linsolve(omkk_g.',gmat.');
B0=2*f_g(1)/(pi);
A0=-1*(1-alpha*Mdim/HBiotdim)*B0/(2*(1-taudry^2));
kappa=1+2*pi*n0*A0;
Q(q)=-2*imag(kappa)/real(kappa);
sigmaP=4*pi*imag(I*k1*A0)/k1;
```

```
sigmaPP(q)=sigmaP;

for i=1:length(f_g)
B_g(i)=2*f_g(i)/(pi);

if u(i)<=k1
    q1=-I*sqrt(k1^2-u(i)^2);
else
    q1=sqrt(u(i)^2-k1^2);
end

q2=-I*sqrt(k2^2-u(i)^2);
AR_g(i,q)=-1*(2*u(i)^2-oo^2*(1-alpha*Mdim/HBiotdim))*B_g(i)/(2*...
(1-taudry^2)*(-1)*oo^2);
A1_g(i,q)=(-1/(alpha*taudry^2*q1))*(-1)*(oo^2*(1-alpha*Mdim/HBiotdim))...
*B_g(i)/(2*(1-taudry^2)*(-1)*oo^2);
A2_g(i,q)=-1*A1_g(i,q)*q1/q2*k2^2*(2*u(i)^2*(k1^2-k0^2)-b*alpha*...
taudry^2*(I*oo^3))/(k2^2*(2*u(i)^2-oo^2)-b*alpha*taudry^2*(I*oo^3));
A3_g(i,q)=(2*u(i)^2*alpha*taudry^2/(2*u(i)^2-oo^2))*(A1_g(i,q)*q1+...
A2_g(i,q)*q2);
rrr=1;

wz_spectrum(i,q)=(-1/(I*oo*bdim))*(A1_g(i,q)*q1*(k0^2-k1^2)+...
A2_g(i,q)*q2*(k0^2-k2^2));
wz_spectrum(i,q)=(-1/(I*oo*bdim))*(A2_g(i,q)*(-k2^2)/(k2/q2)^8);
wr_spectrum(i,q)=wz_spectrum(i,q)/q2;

uz1(i,q)=-1*alpha/Ldim*A1_g(i,q)*q1;
```

```
uz2(i,q)=-1*alpha/Ldim*A2_g(i,q)*q2;
uz3(i,q)=A3_g(i,q);
freq(i,q)=oo;
uarr(i,q)=u(i);
uarrk1(i,q)=u(i)/k1;
uarrkk(i,q)=u(i)/kk;
uarrk3(i,q)=u(i)/k3;

A0_g=-1*(1-alpha*Mdim/HBiotdim)*B_g(1)/(2*(1-taudry^2));
uz0(i,q)=-1*A0_g;

end
end
figure;

plot(uarrkk,wz_spectrum);
grid on;
 axis([0 1 -4 7]);
xlabel('Horizontal Slowness');
ylabel('w_z');
legend('0.0001','0.001','0.01','0.1','1','10','100','1000','10000',0)
%  set(legend,'FontSize',22);

figure;

plot(uarrkk,wr_spectrum.*uarr);
grid on;
  axis([0 1 -0.5 1]);
```

```
xlabel('Horizontal Slowness');
ylabel('w_r');
legend('0.0001','0.001','0.01','0.1','1','10','100','1000','10000',0)
%  set(legend,'FontSize',22);

figure; plot(log10(omegadim),-Q/n0,'*');hold on;
xlabel ('Frequency')
ylabel ('Scattering Cross-section')

grid on;


grid on;
```

B.2 lambdaK_generalf.m

```
function lambdaK_general = lambdaK_generalf(u,z)

global k0 k1 k2 k3 visc perm b bdim I oo Kg mug Kf porosity alpha Kdry;
global mudry taudry L Kstar M HBiot Mdim HBiotdim Ldim rhodrydim;

if z==u
    K=(-1/pi)*(1-sin(z+u)/(z+u));
    else
    K=(-1/pi)*(sin(z-u)/(z-u)-sin(z+u)/(z+u));
end
```

```
k0=oo/sqrt(Ldim);
c1=sqrt(HBiotdim);
k1=oo/c1;
k2=sqrt(I*oo*bdim*HBiotdim/(Ldim*Mdim));
k3=oo;

if u<=k1
    q1=-I*sqrt(k1^2-u^2);
else q1=sqrt(u^2-k1^2);
end

q2=-I*sqrt(k2^2-u^2);

if u<=k3
    q3=-I*sqrt(k3^2-u^2);
else q3=sqrt(u^2-k3^2);
end

H1=1+alpha*Mdim*oo^2/(HBiotdim*(2*u^2-oo^2));
H2=(2*u^2-oo^2)^2-4*u^2*q3*q1-(k1^2-k0^2)*(2*u^2-oo^2)/(alpha*taudry^2);
H3=-2*(1-taudry^2)*oo^2*q1*u;
H4=2*u^2*alpha^2*Mdim-HBiotdim*bdim*alpha*I*oo;
H5=(2*u^2-oo^2)^2-4*u^2*q3*q2-1*k2^2*(2*u^2-oo^2)/(alpha*taudry^2);
H6=2*HBiotdim*(Ldim-1)*q2*u*(-1)*k2^2;
H7=2*u^2-oo^2*(1-alpha*Mdim/HBiotdim);
H=H1*(H2/H3+H4*H5/(H6*H7))-1;

lambdaK_general=K*H*u/z;
```

B.3 gf.m

```
function g = gf(z)

global I kk Kg mug Kf porosity alpha Kdry mudry taudry L Kstar M HBiot;
global Mdim HBiotdim Ldim;

T=(sin(z)-z*cos(z))/z^3;
p=-1*(HBiotdim-alpha*Mdim);
g=p*T;
```

Appendix C

Chapter 5 MATLAB Code

This appendix contains the MATLAB code used to produce the results of Chapter 5. "sparsedistribution.m" uses the single scattering solution from "singlescattering.m" to calculate the effective properties of a medium containing a sparse distribution of cracks. Note that this code also refers to the function files "lambdaK_generalf.m" and "gf.m".

C.1 sparsedistribution.m

```
clear all;

global I kk Kg mug Kf porosity alpha Kdry mudry taudry L Kstar M;
global HBiot Mdim HBiotdim Ldim;

I=sqrt(-1);
n0=0.01;
Kg=37*10^9;
mug=44*10^9;
Kf=2.25*10^9;
porosity=0.3;
```

```
alpha=1-(1-porosity)^(3/(1-porosity));
Kdry=Kg*(1-alpha);
mudry=mug*(1-alpha);
L=Kdry+4*mudry/3;
taudry=sqrt(mudry/L);
M=Kg/((1-Kdry/Kg)-porosity*(1-Kg/Kf));
HBiot=L+alpha^2*M;
tausat=sqrt(mudry/HBiot);
Mdim=M/mudry;
HBiotdim=HBiot/mudry;
Ldim=L/mudry;
Kfdim=Kf/mudry;
N=4;
fspac=0.15;
NN=N/fspac;

for i=1:1:NN
ord=(i-1)*fspac-1;
  k(i)=10^ord;
end

for q=1:length(k)
    kk=k(q);

k2=-kk*sqrt(I)*I;
x1=0;
if kk <= 1
   spac=2*kk;
```

```
  x2=4;
   x2=200*spac;
   spac=0.1*kk;
else
   spac=0.002*kk;
   x2=40;
end

x2=max(4,kk*10);
p=-1*(HBiotdim-alpha*Mdim);

NMAX=200;
omk=eye(NMAX);

% CALCULATE GAUSS-LEGENDRE WEIGHTS

m=(NMAX+1)/2;
xm=(x2+x1)/2;
xl=(x2-x1)/2;

for i=1:m
    Z=cos(pi*(i-1/4)/(NMAX+1/2));
    Z1=Z-1;
    while (Z-Z1) > 3d-14
    p1=1;
    p2=0;
    for j=1:NMAX
        p3=p2;
```

```
        p2=p1;
        p1=((2*j-1)*Z*p2-(j-1)*p3)/j;
    end

    pp=NMAX*(Z*p1-p2)/(Z^2-1);
    Z1=Z;
    Z=Z1-p1/pp;

    end
        x(i)=xm-xl*Z;
        x(NMAX+1-i)=xm+xl*Z;
        w(i)=2*xl/((1-Z^2)*pp^2);
        w(NMAX+1-i)=w(i);
end



for i=1:NMAX
    u(i)=x(i);

end

    for j=1:NMAX
        z(j)=x(j);
    end

    for i=1:NMAX
        for j=1:NMAX
```

```
            omkk(i,j)=omk(i,j)-lambdaKf(u(i),z(j))*w(i);
    end
end

for j=1:NMAX
    gmat(j)=gf(z(j));

end

f=linsolve(omkk',gmat');
B0=2*f(1)/(pi);
A0=-1*(1-alpha*Mdim/HBiotdim)*B0/(2*(1-taudry^2));
kappa=1+2*pi*n0*A0;

% Complicated asymptote
%kappaAlowf=1-2*n0*(HBiotdim-alpha*Mdim)*(-1/3*HBiotdim+1/3*...
% alpha*Mdim+1/30*(HBiotdim-alpha*Mdim)*Mdim*k2^2*(2*Ldim^2+3*...
% alpha^2-4*alpha*Ldim)/(HBiotdim*(Ldim-1)*(1+1/8*Mdim*k2^2*...
% (2*Ldim^2+3*alpha^2-4*alpha*Ldim)/(HBiotdim*(Ldim-1)))))/...
% (HBiotdim*(1-taudry^2));
% Simple asymptote
kappaAlowf=1-2*n0*(HBiotdim-alpha*Mdim)*(-1/3*HBiotdim+1/3*alpha...
*Mdim+1/30*(HBiotdim-alpha*Mdim)*Mdim*k2^2*(2*Ldim^2+3*alpha^2-...
4*alpha*Ldim)/(HBiotdim*(Ldim-1)*(1)))/(HBiotdim*(1-taudry^2));

% Complicated asymptote
%kappaAhighf=1-2*n0*(HBiotdim-alpha*Mdim)*(-1/3*HBiotdim+1/3*...
% alpha*Mdim+1/3*(HBiotdim-alpha*Mdim)*Mdim*Ldim^2*k2/(HBiotdim...
```

```
% *(Ldim-1)*(1+Mdim*Ldim^2*k2/(pi*HBiotdim*(Ldim-1)))*pi))/(...
% HBiotdim*(1-taudry^2));
% kappaAhighf=1+2/3*n0*(HBiotdim-alpha*Mdim)^2*(-HBiotdim+...
% alpha*Mdim)*pi*(Ldim-1)/k2/(Mdim*Ldim^2*(1-taudry^2));
% Simple asymptote
% kappaAhighf=1-2/3*n0*(HBiotdim-alpha*Mdim)*(-HBiotdim+alpha*...
% Mdim)*pi*(Ldim-1)/(Mdim*Ldim^2*(1-taudry^2))/k2;
kappaAhighf = 1+pi*n0*(-HBiotdim+alpha*Mdim)^2/(Ldim*Mdim*k2);

J=sqrt(porosity*Kfdim*HBiotdim/(kk^2*2*Ldim*Mdim));
KH=((1+I)/3)*Ldim*(Kfdim/(Ldim-1))*(1/J);
kappaH=1/sqrt(1-(4/3)*Ldim^2*n0/((Ldim-1)*(1+KH)));

KKH(q)=abs(KH);
JJ(q)=1/J^2;
v(q)=1/real(kappa);
vH(q)=1/real(kappaH);

vlow(q)=1/real(kappaAlowf);
vhigh(q)=1/real(kappaAhighf);

Q(q)=-2*imag(kappa)/real(kappa);
QH(q)=-2*imag(kappaH)/real(kappaH);
Qlow(q)=2*imag(kappaAlowf)/real(kappaAlowf);
Qhigh(q)=2*imag(kappaAhighf)/real(kappaAhighf);
QHhigh(q)=2*n0*Ldim*J/(Kfdim);

end % Frequency (q) loop
```

```
 figure; semilogx((k.^2),(v),'k *',k.^2,vlow,k.^2,vhigh,'--'...
 ,k.^2,vH,'.');grid on;
% axis([ 1e-2 1e6 0.975 1.005]);

  xlabel('Frequency')
  ylabel('Velocity')
hold on;

 plot(log10(k.^2),log10(Q),'k *',log10(k.^2),log10(Qlow),'o',...
 log10(k.^2),log10(Qhigh),'--',log10(k.^2),log10(QH),'.');grid on;
axis([ -2 6 -5 -1 ]);
```